Heat transfer study of enhanced additively manufactured minichannel heat exchangers

Hamidreza Rastan[a,*], Amir Abdi[a], Bejan Hamawandi[b], Monika Ignatowicz[a], Josua P. Meyer[c], Björn Palm[a]

[a] *Department of Energy Technology, KTH Royal Institute of Technology, SE-100 44, Stockholm, Sweden*
[b] *Department of Applied Physics, KTH Royal Institute of Technology, SE-106 91, Stockholm, Sweden*
[c] *Department of Mechanical and Aeronautical Engineering, University of Pretoria, Hatfield, Pretoria, South Africa*

Abstract

Three-dimensional (3D) printing, known as additive manufacturing, provides new opportunities for the design and fabrication of highly efficient industrial components. Given the widespread use of this technique by industries, 3D printing is no longer limited to building prototypes. Instead, small-to-medium scale production units focus on reducing the cost associated with each part. Among the various industrial components that can be developed with this manufacturing technology are heat transfer components such as heat exchangers. To this end, this study investigated the heat transfer characteristics of minichannel-based heat exchangers embedded with longitudinal vortex generators, both experimentally and numerically. Three enhanced prototypes with different vortex generator design parameters and a smooth channel as a reference case were printed with an aluminum alloy (AlSi10Mg)

*Corresponding author
Email address: hamras@kth.se (Hamidreza Rastan)

Preprint submitted to International Journal of Heat and Mass Transfer

using direct metal laser sintering (DMLS). The rectangular minichannel had a hydraulic diameter of 2.86 mm. Distilled water was used as the test fluid, and the Reynolds number varied from 170 to 1,380 (i.e., laminar flow). Prototypes were tested under two different constant heat fluxes of 15 $\mathrm{kW\,m^{-2}}$ and 30 $\mathrm{kW\,m^{-2}}$. The experimental results were verified with a commercial simulation tool, Comsol Multiphysics®, using the 3D conjugate heat transfer model. In the case of the smooth channel, the experimental results were also compared with well-known correlations in the field. The results showed that 95% and 79% of the experimental data were within 10% of the numerical simulation results and the values from the existing correlations, respectively. For the channel enhanced with the vortex generators, the numerical predictions agreed well with the experimental results. It was determined that the vortex generators can enhance the convective heat transfer up to three times with the designed parameter. The findings from this research underline the potential of additive manufacturing in the development of more sophisticated minichannel heat exchangers.

Keywords: minichannel, microchannel, additive manufacturing, 3D printing, vortex generator, numerical simulation

---

Nomenclature

Acronyms

DMLS	Direct metal laser sintering
EBM	Electron beam melting
FEM	Finite element method
HX	Heat exchanger
PEC	Performance evaluation criteria
RMS	Root-mean-square
VG	Vortex generator

Roman Symbols

$A_{planform}$	Minichannel top surface area [m^2]
A_{wetted}	Convective heat transfer area (per channel) [m^2]
a	Channel width [m]
b	Channel height [m]
c_p	Specific heat [$J\,kg^{-1}K^{-1}$]
D_h	Hydraulic diameter [m]
d_{wall}	Distance between side wall and closest vortex generator tip [m]
E	Electrical power [W]
H	Height of vortex generator [m]
$\bar{h}$	Average convective heat transfer coefficient [$W\,m^{-2}K^{-1}$]

I	Current [A]
k	Thermal conductivity [$\mathrm{W m^{-1} K^{-1}}$]
L	Channel length [m]
l	Length of vortex generator winglet [m]
$l^{'}$	Distance from channel inlet to the first longitudinal vortex generator winglet downstream tip [m]
$\dot{m}$	Mass flow rate [$\mathrm{kg\,s^{-1}}$]
P	Pressure [Pa]
$\dot{Q}_{sensible}$	Sensible heat gain [W]
$\dot{Q}_{loss}$	Heat loss from the system [W]
$q^{''}$	Heat flux based on planform area [$\mathrm{W m^{-2}}$]
R_a	Arithmetic mean roughness [μm]
R_q	Root-mean-square roughness [μm]
S	Longitudinal pitch [m]
s	Distance between measured surface temperature and inner channel wall [m]
T	Temperature [K]
$\overline{T}_{fluid}$	Mean fluid temperature [K]
$\overline{T}_{wall}$	Mean wall temperature [K]
t	Channel wall thickness [m]
u	Velocity [$\mathrm{m\,s^{-1}}$]

V	Voltage $[\mathrm{kg\,m^2\,A^{-1}\,s^{-3}}]$
VG	Vortex generator
w	Thickness of the vortex generator [m]
x, y, z	Cartesian coordinates

Dimensionless numbers

f	Friction factor
Gz_D	Graetz number
N	Number of rectangular minichannels per flat tube
Nu	Nusselt number
Pr	Prandtl number
Re	Reynolds number
U	Uncertainty
x^+	Hydrodynamic axial distance
x^*	Thermal axial distance

Greek Symbols

α	Channel aspect ratio $[-]$
β	Angle of attack $[^\circ]$
μ	Dynamic viscosity $[\mathrm{kg\,m^{-1}\,s^{-1}}]$
ρ	Density $[\mathrm{kg\,m^{-3}}]$

Subscripts

app	Apparent

blk	Bulk
in	Inlet
m	Mean
out	Outlet
s	Smooth

1. Introduction

The increase in the global population and improvements in living conditions due to technological progress and economic growth have escalated the global energy demand. According to a report released by British Petroleum in 2019 [1], energy systems worldwide will encounter dual challenges as the energy demand is predicted to grow by one-third between 2019 and 2040; further, carbon emissions will have to decrease to contain global warming. Therefore, to ensure a sustainable environment for future generations, societies must devote considerable effort not only to replace inexpensive oil and gas with renewable technologies, but also to increase the energy efficiency of processes that use conventional resources [2, 3]. The latter option seems more plausible in the short term for a smooth transition toward the final goal, namely a complete conversion to renewable technologies [4].

Among energy systems/subsystems, heat exchangers (HXs) can play a crucial role in saving energy mainly because of their widespread use in different industries. The use of high-performance HXs can be considered as one option to increase the efficiency of energy-intensive industrial processes [5]. Mini/microchannels are one of the common types of HXs. These HXs

have a higher thermal performance than conventional tubes due to a larger surface-to-volume ratio that can lead to compact HXs if they are designed properly.

Mini/microchannel components have been studied by researchers since the early 1980. According to the fixed metrics introduced by Kandlikar [6], channels/tubes have been classified in terms of their hydraulic diameter D_h and their associated applications. Kandlikar divided tubes into three different groups. Channels/tubes with a D_h exceeding 3 mm are termed conventional channels, while those with a D_h ranging from 0.2 to 3 mm and 0.01 to 0.2 mm are called minichannels and microchannels, respectively. This field of research was pioneered by Tuckerman and Pease [7]. They proposed the idea of using forced convection of liquid water through small rectangular passages to remove excessive heat produced by electronic devices. Tuckerman and Pease showed that their designed microchannel heat sink was able to dissipate 790 W from a 1 cm^2 silicon wafer by expending 213 kPa drop in pressure. The work by Tuckerman and Pease served as the starting point for other researchers in the field. Other researchers have explored the same configuration in more detail and made an effort to enhance the design analytically, numerically, or experimentally [8–12]. Even though early studies have focused on the cooling of electronics, the applicability of the idea was extended to other areas, including low-charge refrigeration units and microfluidic devices [13–15].

To lower the thermal resistance and to accommodate higher heat fluxes, various techniques have been suggested in order to augment the heat transfer in single- or two-phase flow. Bergles [16] categorized the heat transfer en-

hancement methods into the passive, active, and compound forms, which can potentially improve the energy performance as well as reduce the size and the manufacturing costs [17, 18]. While passive techniques do not require external power to intensify the heat transfer, which are based on geometrical modifications or fluid additives, active methods require an external power. The HX's structural vibrations, fluid vibrations, and electrostatic field are examples of the active methods. Techniques that simultaneously use more than one method are referred to as compound techniques. From a practical perspective, passive techniques are favorable due to their ease of implementation and lower maintenance requirements.

Using laminar single-phase flow in mini/microchannels is of particular value in many industrial applications because it can avoid corrosion induced by turbulent flow and the associated high pressure drop. However, the thermal exchange rate is inevitably lower within the laminar flow range. Therefore, passive techniques can be practiced to enhance the heat transfer. Among the different passive methods, embedding vortex generators (VGs) are widely adopted for external and internal flows. VGs enhance the convective heat transfer through boundary layer interruption, the generation of vortices, and the destabilization of flow [19]. As flow passes through the VG, three-dimensional (3D) vortices are generated due to the pressure difference between the two sides of the VG. Depending on the angle of attack and the Reynolds number, the vortices can be mainly produced in the streamwise direction (longitudinal vortices) or in the spanwise and normal directions (transverse vortices). Using VGs, turbulence promoters (sometimes known as turbulators) will generate a swirl in the primary direction of the flow

[20]. The generated stream-wise vortices take the heated near-wall fluid and bring it up to the center of the vortices, thereby mixing it with the cold free stream fluid and enhancing the heat transfer. In addition, the generated longitudinal vortices avoid the growth of boundary layers by pushing them down and causing a thinning effect [21]. It is well established that longitudinal vortices enhance the global heat transfer due to their existence over long downstream distances of the VG [22–24]. In contrast, transverse vortices usually cause flow destabilization in the small wake region behind the VG tail; thus, enhancing the convective heat transfer locally. It is favorable to have stream-wise vortices as transverse vortices lead to pressure loss with local heat transfer improvement. However, it is impossible to generate pure longitudinal vortices. Transverse vortices are always generated simultaneously. Wing-type VGs have four typical configurations: rectangular wing, rectangular winglet, delta wing, and delta winglet (see Fig. 1(c)).

While early heat transfer research on VGs was related to the external flow [26], researchers have attempted to embed VGs inside channels to lower the thermal resistance of the gas in fine-tube HXs or to remove high heat fluxes. For example, Fiebig [20] compared the effect of different VG configurations on the heat transfer and pressure loss inside a rectangular channel with a hydraulic diameter of 33 mm. Using air as the working fluid under a transitional turbulent flow regime, he concluded that winglet-type VGs provided better overall results (in terms of the ratio of the heat transfer enhancement to increase in pressure loss) in comparison to the wing type. Further, it was reported that the optimum angle of attack β was 65° for all of the studied configurations. Moreover, his results showed that the effect

of applying the VG was more pronounced for a lower Reynolds number. In another study, Fiebig et al. [27] investigated the performance of wing-type VGs on the heat transfer and the pressure drop inside a rectangular channel under developing laminar conditions. A number of plate fins were stacked together to form a channel, and the single VGs were embedded on each plate fin. The Reynolds number varied between 1,000 and 2,000 and air was the working fluid. Using the liquid crystal thermography method to measure the local heat transfer, they reported a local heat transfer augmentation of 100% and an average heat transfer enhancement of more than 50%. The results indicated the existence of longitudinal vortices up to 50 times the area of the VG downstream. Wu and Tao [28, 29] numerically investigated the effects

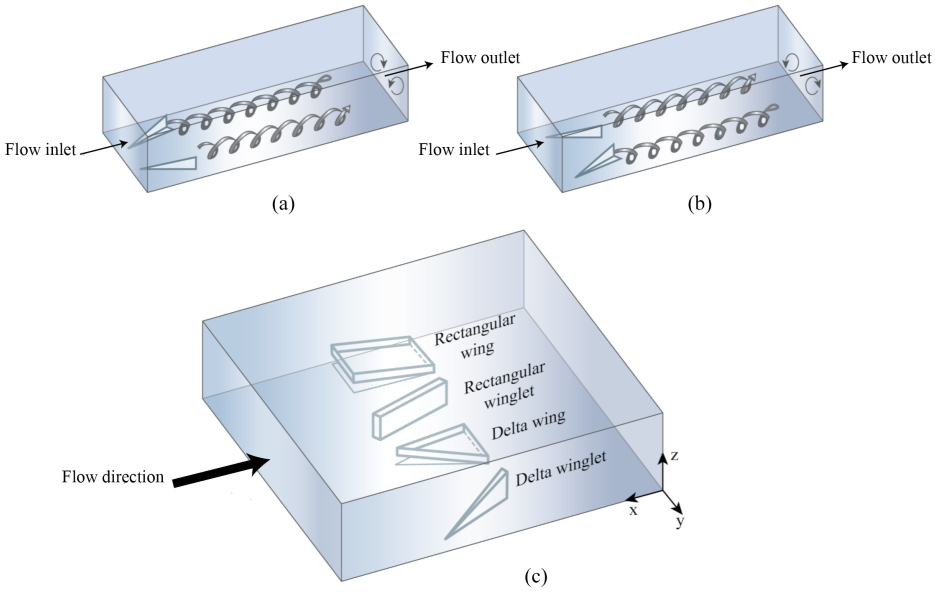

Figure 1: Different VG arrangements and formations: (a) inflow pair, (b) outflow pair, (c) common vortex generator configurations. Adapted from [25].

of the VG design parameters on the heat transfer and the flow friction in a channel. Using the so-called field synergy principle, they indicated that the VGs with an attack angle of 45° produced the highest effectiveness within a laminar flow range. Moreover, they found that an excessive reduction of the transverse pitch of the VG caused interactions between the main vortices and decreased the heat transfer enhancement. Liu et al. [30] experimentally studied the single-phase flow characteristics of an embedded rectangular VG inside a microchannel with a hydraulic diameter of 187.5 μm. They examined the impact of the number of VGs and the angle of attack on the heat transfer and the flow friction. Using water as the working fluid, a lower value of the critical Reynolds number for the transition flow ($Re = 700$) was reported when a VG was used. They reported 9% to 21% higher heat transfer in comparison to the plain microchannel in the laminar flow range and 39% to 90% enhancement for the turbulent flow. The same research group [31] extended their previous work by analyzing the effect of the VG height and the aspect ratio on the heat transfer and the flow friction characteristics. Three sides of the microchannel were maintained at a constant temperature, and Reynolds number ranged from 350 to 1,500. The results indicated a heat transfer enhancement of 12% to 74% with a corresponding increase of 40% to 154% in the pressure drop for a microchannel with an aspect ratio of 0.0667 equipped with a rectangular wing. Datta et al. [32] numerically studied the influence of the angle of attack and the number of VG pairs in laminar flow using deionized water as the working fluid. The authors declared that the best overall performance was obtained when the VGs were inclined at 30° to the flow direction for a Reynolds numbers above 600. Recently, using finite

volume-based numerical simulation, Ebrahimi et al. [33] analyzed the laminar flow inside a microchannel equipped with two rows of VGs. Except for one case and when the Reynolds number was equal to 100, a higher overall HX efficiency was obtained for all the other investigated cases.

Another important aspect of the micro/minichannel components concerns the fabrication. Microchannel heat sinks are typically manufactured through one of two approaches. The first approach entails conventional fabrication techniques—such as milling, sawing, electrical discharge machining, and water jet cutting—implemented on a micro scale. The second approach entails microfabrication methods emerged from the semiconductor industry, such as etching and lost wax molding [34]. In both approaches, channels are produced on silicon or metal substrates with high thermal conductivity. Therefore, building single monotonic heat sinks is not feasible, and a lid is required to complete the assembly and seal it. An extrusion process is typically used to produce multiport minichannel-based HXs. However, all of the manufacturing approaches listed above suffer from geometric constraints. Constructing complex out-of-plane features is extremely difficult and time-consuming, and in some instances impossible [35]. These manufacturing restrictions can be eliminated through the use of additive manufacturing (AM), generally known as 3D printing.

3D printing is a new manufacturing approach in which the objects are built layer by layer. This method is environmentally advantageous over conventional practices such as subtractive manufacturing since the left-over materials can be reused. From an economic point of view, the price of a manufactured part will not usually increase with higher production complexity;

however, the opposite applies to other technologies that require relatively more labor. Given the considerable industrial interest in this technique, AM is no longer limited to building prototypes; rather, small-to-medium scale production units aim to reduce the cost per part. However, a number of limiting factors hinders the extensive usage of AM in various industries. This includes a higher cost in comparison to ordinary manufacturing methods, the need for geometric accuracy and part repeatability, a limited number of materials, a lack of comprehensive material standards, and a high surface roughness [36, 37]. Among the commercially available metal additive technologies, two methods, electron beam melting (EBM) and direct metal laser sintering (DMLS), appear to be promising in HX design. The results of the production of a small prototype at the KTH Royal Institute of Technology (see Appendix A) indicate that the DMLS is favorable in developing heat transfer components mainly because of its lower surface roughness, improved geometrical uniformity, and broad material choices. Various metal alloys such as aluminum, titanium, Inconel, and stainless steel are used in 3D printing. Among them, aluminum alloy (AlSi10Mg) is interesting because of its high thermal conductivity and light weight.

The literature on AM of mini/microchannels is currently limited owing to the fact that AM is a relatively new fabrication method. Kirsch and Thole [38], for example, studied heat transfer and pressure loss in additively manufactured wavy microchannels. Three test coupons with different wavelengths and a smooth channel as a benchmark were printed in Inconel 718 as parts of the cooling passages of hot turbine components with DMLS technology. Using air as the working fluid, the authors concluded that the short wavelength

channels led to a high pressure drop without considerable heat transfer augmentation. For the same friction factor, longer wavelength channels resulted in a considerable increase in the Nusselt number Nu compared with the reference case. Finally, it was concluded that the heat transfer enhancement was higher for Reynolds numbers below 4,000. In another study [39], the same authors investigated the possibility of embedding cylindrical pin fins inside microchannels. Four different prototypes with various spanwise and streamwise spaces were printed using the DMLS technique with Inconel 718. They reported an extremely high surface roughness and distorted shapes as the number of pins increased. Furthermore, the results of the pressure drop and the heat transfer enhancement showed that fewer pin fin arrays may lead to a better overall HX performance. This could be attributed to the flow structure and the higher surface roughness as the number of pin fins increased. A comparison of the two studies showed that the wavy channels outperformed the pin fin arrays for lower Reynolds numbers. Arie et al. [40] studied the feasibility of implementing AM to develop microchannels for dry cooling in power plants. Three test sections with the same geometry were printed in stainless steel (SS17-4), titanium alloy (Ti64), and aluminum alloy (AlSi10Mg). The authors reported that titanium alloy exhibited the best geometrical accuracy when compared with the intended designed dimensions. When the Reynolds number was 400, the overall heat transfer coefficient (U) was $1\,700\ \mathrm{W\,m^{-2}\,K^{-1}}$, $1\,100\ \mathrm{W\,m^{-2}\,K^{-1}}$, and $3\,000\ \mathrm{W\,m^{-2}\,K^{-1}}$ for SS-17, Ti64, and AlSi10Mg, respectively. They concluded that their manifold microchannel in the cross-flow configuration could improve the overall performance by up to 30% and 40% in comparison to conventionally manufactured wavy fin

and plain plate fin HXs, respectively. Collins et al. [37] recently analyzed the single-phase flow in a microchannel that was additively manufactured for electronics cooling. The microchannels consisted of 16 identical channels with a square-shaped cross-section, and they each had a hydraulic diameter of 0.5 mm. After printing and testing the section in AlSi10Mg using DMLS technology, they found a mismatch between the experimental heat transfer results and those of the laminar model, which they attributed to unknown thermal alloy properties. In addition, the authors reported an early transition to turbulent flow at a Reynolds number of approximately 500.

The present study investigated the effect of a longitudinal VG in additively manufactured minichannel HXs, both experimentally and numerically. Three test sections with different VG design parameters and a smooth channel (as a reference) were printed in AlSi10Mg using the DMLS method. Each test section consisted of eight channels of rectangular cross-section, the designed hydraulic dimensions being 2.86 mm. Distilled water was used as the working fluid, the Reynolds number varied within a laminar flow range ($170 < Re < 1{,}380$), and two different heat fluxes (15 $\mathrm{kW\,m^{-2}}$ and 30 $\mathrm{kW\,m^{-2}}$) were applied from the top wall of the HX. Another experiment was performed to assess the material properties of the aluminum alloy, which were required for accurate thermal measurement. The results of the experiment were compared with well-known correlations within the field for the smooth channel as well as the numerical solution obtained from the commercial finite element method (FEM)-based software, COMSOL Multiphysics®.

2. Experimental Analysis

An experimental setup was designed and constructed to analyze the single-phase thermal characteristics of additively manufactured minichannel HXs. Distilled water was used as the working fluid, and minichannel HXs were tested under constant heat flux boundary conditions in the laminar flow range. In the case of the smooth channel, considering the test-rig configuration, the tested flow range, and the working fluid, the flow would either be simultaneously developing or thermally developing. The criteria is that the hydrodynamic axial distance ($x^+ = L(D_h Re)^{-1}$) and the thermal axial distance ($x^* = L(D_h RePr)^{-1}$) should have values above 0.05 for fully developed conditions to be met [41, 42]. In this study, only at the lowest tested Reynolds number, flow became fully developed at the outlet.

2.1. Flow loop

Figure 2 demonstrates the experimental facility used to measure the heat transfer characteristics of the 3D-printed minichannel HXs. The schematic layout of the flow loop is shown in Fig. 3. To explain the flow loop and starting before the gear pump, a column of distilled water was installed to exert extra pressure. This facilitated the venting process and ensured that the system operated above the atmospheric pressure. It also served the purpose of system charging. The working fluid (distilled water in this study) was circulated through the main loop by a gear pump (ISMATEC, MCP-Z Standard) driven by a microprocessor control. The pump provided a wide range of flow rates, from a minimum of 1 $\mathrm{mL\,min^{-1}}$ to a maximum of 7,020 $\mathrm{mL\,min^{-1}}$. A custom-made mica heater (Backer Calesco®) of to-

tal thickness 2 mm, powered by a DC electrical power unit equipped with a PID controller (Eurotherm 2404), was used to heat the water as it flowed through the test module. Since the test module was designed as a closed loop, the heated water needed to be cooled to the minichannel inlet temperature; this was achieved using a plate heat exchanger (SWEP) and a thermal bath (LAUDA, RE204). When high heat flux was applied, an additional plate heat exchanger was connected to the loop, cooling the working fluid with tap water. Finally, the water passed through a turbine and a Coriolis flow meter. The facility was equipped with the necessary instrumentation to measure the heat characteristics of the HX. Two resistance temperature detectors (RTDs) measured the bulk temperature of the working fluid. Additional thermocouples were installed to ensure the correct measurement of the fluid temperature. Multiple thermocouples were positioned to measure the minichannel wall temperature. Turbine and Coriolis flow meters with different measurement ranges were used for the accurate measurement of the circulating flow rate in the main loop. Measurements were taken in the primary loop, in which components were connected to each other by a stainless steel tubing (6 mm outer diameter and a 1 mm wall thickness). In the other loops, components were connected using plastic hoses. A Swagelok tube fitting and plug valves, which can withstand high pressures, were installed before and after the test module. Note that the pipes in the primary loop, especially the test module, were well insulated with Armaflex® synthetic rubber, which has an extremely low thermal conductivity ($k < 0.042\ \mathrm{W\,m^{-1}\,K^{-1}}$).

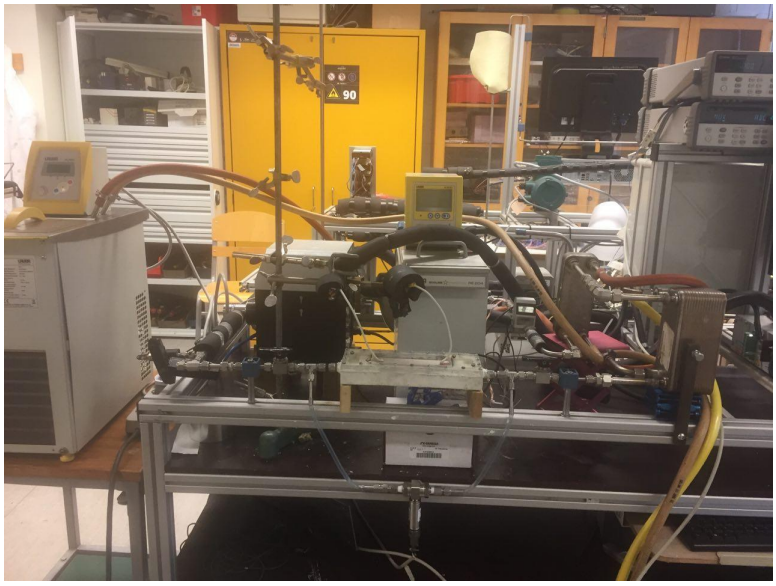

Figure 2: Photograph of the experimental test-rig.

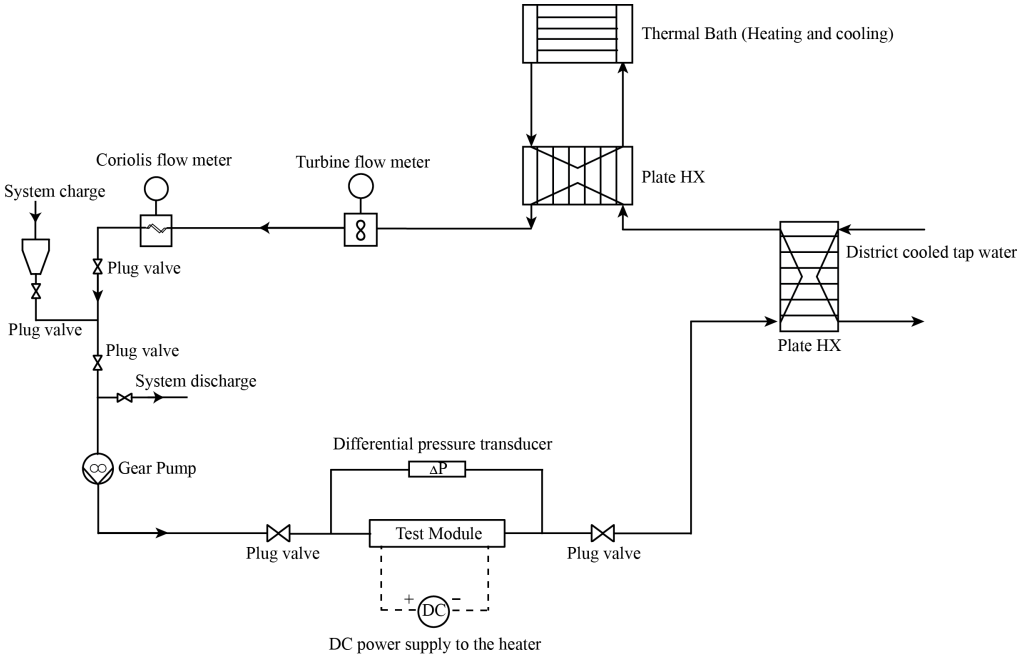

Figure 3: Schematic representation of the test-rig.

2.2. Test module

The exploded view of the test module is shown in Fig. 4. The main components of the test module were the housing, the minichannel HX, the cover plate, and the mica heater. The HX housing was 3D printed and sealed in polylactic acid (PLA). PLA was selected because of its low thermal conductivity ($k \approx 0.13$ $\mathrm{W\,m^{-1}\,K^{-1}}$), which ensured a low heat loss to the surroundings during the experiment. The housing contained plenums upstream and downstream of the minichannel. Each plenum consisted of a deep portion leading to a shallow portion to facilitate an even distribution of flow between the minichannels and good mixing at the exit. Thus, the working fluid bulk temperature reading could be enhanced. This design was applied successfully in several previous studies, including that of Qu and Mudawar and Khsohvaght-Aliabadi et al. [9, 43]. Two four-wire RTDs from Pentronic® with an accuracy of 1/10 DIN were placed at the deep portion of the plenums to measure the inlet and outlet temperatures of the working fluid. The minichannel HX prototypes were additively manufactured with AlSi10Mg by using DMLS technology. Among the commercially available materials for 3D metal printing, AlSi10Mg was chosen due to its superior mechanical and thermal performance over the other existing alloys. As illustrated in Fig. 5, the flat tube prototypes consisted of eight rectangular channels, each with designed width a and height b of 5 mm and 2 mm, respectively, and they were separated by a wall thickness t of 1.2 mm. The minichannel length L was set to 150 mm. Further, 1.5 mm below the top surface of the HX, hereinafter known as the planform area, five 0.6 mm diameter holes were drilled into the side wall of the HX up to the center plane

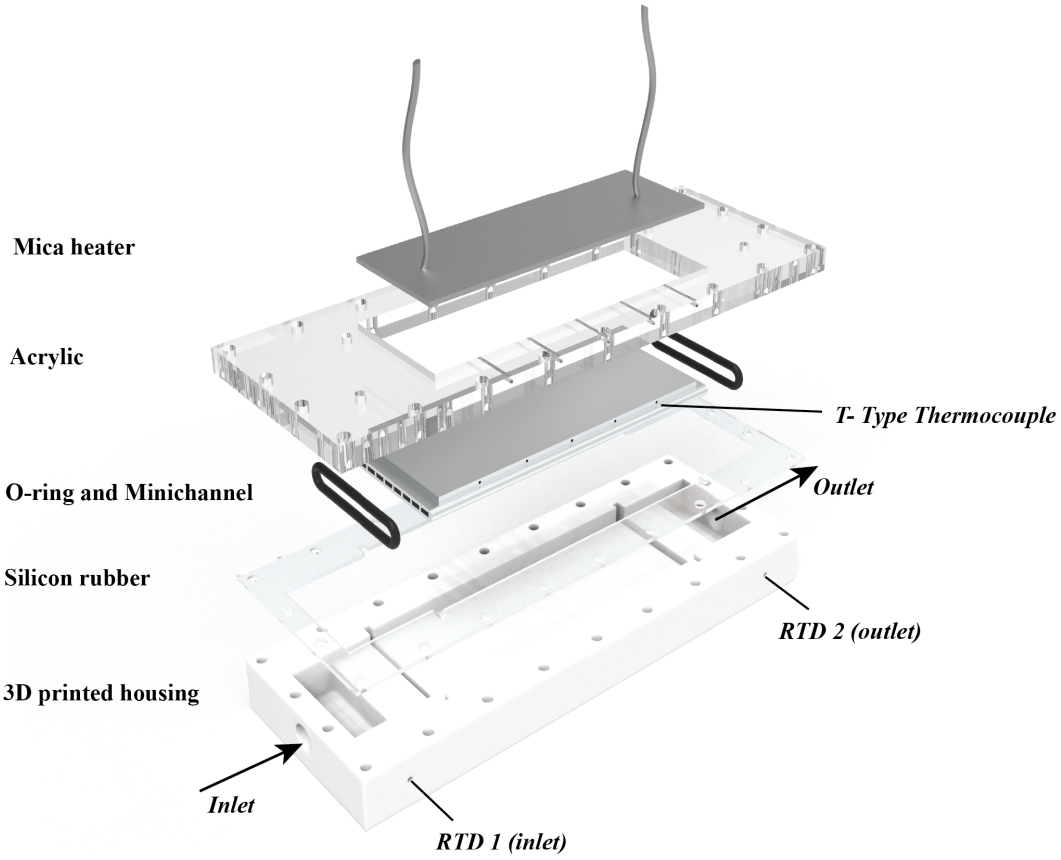

Figure 4: Test module.

(e.g. 24.2 mm of depth). High-quality copper-constantan thermocouples (T-type) from Omega Engineering with a bead diameter of 0.5 mm were inserted into these holes to measure the temperature distribution along the channel length. Thin wire thermocouples were selected to achieve a shorter response time. The thermocouples were placed at a distance of 24 mm away from each other (Fig. 5(b)). To minimize the effect of trapped air inside the holes on the thermocouple readings and to measure the surface temperature more accurately, the holes were filled with a thermal compound (Arctic Silver®

5) with a thermal conductivity of 8.9 $\mathrm{W\,m^{-1}\,K^{-1}}$. Acrylic was used for the cover plate. The central part of the cover plate was removed to accommodate the mica heater. The cover plate was bolted to the housing to fix the minichannel that was in place. Four screws at the inlet and outlet were specifically designed for manual venting. Silicon rubber was attached along the interface between the cover plate and the housing to prevent leakage. In addition, two O-rings were used to ensure that the channel inlet and outlet were sealed. A 260 W custom-made mica heater (2 mm thickness) placed on the top planform area was powered by a DC power unit (EA-PSI 9080-100). This DC power unit had a rated power of 3 kW, which allowed fine voltage and current adjustments. Special attention was given to the heater design so it can dissipate the heat as evenly as possible. The planform area was polished manually using sandpaper and a thin layer of a thermal compound was employed between the heater and the minichannel to ensure a complete attachment. Finally, thin plywood (3 mm thickness) was sandwiched between the insulation material and the heater by using two clamps to avoid the possibly bending or burning out of the heater.

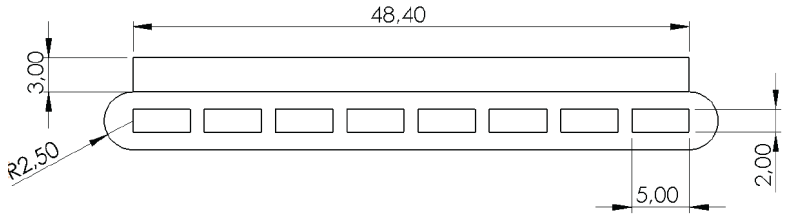

(a)

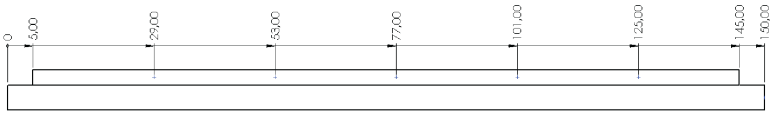

(b)

Figure 5: Details of the minichannel HX dimensions. Dimensions are in (mm).

2.3. Test section

Four prototypes, including the smooth channel as a reference, were manufactured using DMLS technology. In the view of previous experiences with 3D printing (see Appendix A), DMLS is more effective in comparison to the other methods such as EBM in terms of the design uniformity, geometrical accuracy, and the surface roughness. The minichannels were designed and printed based on the results of a numerical study [44] and the machine accuracy (Appendix B). In the aforementioned study, Rastan et al. [44] conducted a numerical parametric study on the effect of the embedded VGs inside a minichannel HX under laminar flow conditions. Their results showed that the angle of attack, VG height, VG length, and the longitudinal pitch had the most significant effects on the heat transfer and the flow friction characteristics. In contrast, the VG thickness and the distance from the sidewalls had a minor influence on the performance of the HX. Therefore, in this investigation, the VG thickness and the distance from the side walls were

fixed based on the capability and limitations of the commercial 3D printing machine in order to fabricate the rectangular winglet VGs accurately. For instance, low thickness can cause VG shape distortion while high thickness may result in flow blockage due to the unmelted powder attaching the VGs to the side walls (see Fig. 23). Also, by considering fixed values for the thickness and the distance from the side walls, other parameters having considerable effects on HX performance could vary within wider ranges due to the channel space limitation. The distance of the first VG from the inlet were fixed in order to avoid the growth of boundary layer. For selection of other parameters, Taguchi method [45] was implemented and combination sets of parameters which yielded to the highest HX performance (ratio of enhanced heat transfer to the increased pressure drop in comparison to smooth tube) were further on selected to be manufactured additively. It should be noted that the design parameters demonstrated in Fig. 6 and summarized in Table 1 were repeated for all eight channels in each test section. All of the other major design parameters of the minichannel (e.g. channel width and channel height) remained the same as presented in Fig. 5.

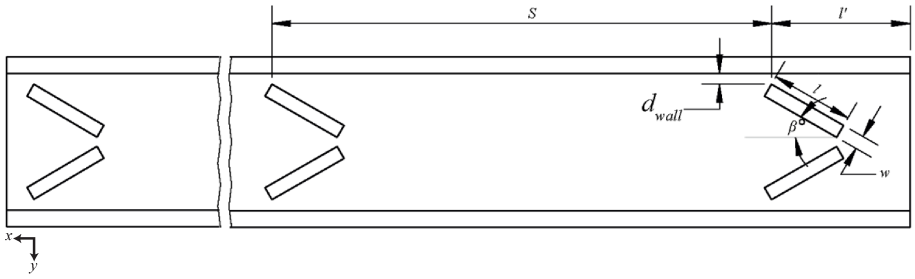

Figure 6: Vortex generator design parameters.

Table 1: Test section designed values.

Symbol	Definition	1(*smooth*)	2	3	4
$l^{'}$	Distance of the first VG row from the inlet	-	5 mm	5 mm	5 mm
l	VG length	-	3 mm	2 mm	2.5 mm
β	Angle of attack	-	30°	45°	30°
H	VG height	-	1.2 mm	1.2 mm	0.8 mm
S	Longitudinal Pitch	-	18 mm	17 mm	22.5 mm
w	VG thickness	-	0.5 mm	0.5 mm	0.5 mm
d_{wall}	Distance from the inner wall	-	0.4 mm	0.4 mm	0.4 mm

2.4. Material properties

The material properties of the used alloy in the experiment (AlSi10Mg) were required in order to correctly evaluate the thermal performance of the 3D-printed prototypes. Therefore, the density, specific heat, and thermal conductivity of the alloy were measured. To achieve this, two cylinders with a diameter of 50 mm and height of 20 mm were printed in the same printing processes that were performed for the prototypes. A digital scale and Vernier caliper were used for the density measurement whereas differential scanning calorimetry (DSC) and the transient plate source method (TPS) were used for the specific heat and thermal conductivity measurement, respectively. The detailed explanation of the measurement is published in [46]. In order to avoid repetition, only the summary of the results is presented in Table 3. Also, the fabrication process of minichannels via 3D printing technique may result in high surface roughness. Surface roughness of each test section were measured using a stylus profiler (KLA-Tencor P-15). The obtained results indicated that prototype 1 (e.g smooth channel) had the highest surface roughness with the arithmetic mean roughness R_a, and the root-mean-square (RMS) roughness R_q of 17.28 μm and 23.40 μm, respectively. See Appendix C for further details.

3. Experimental Data Acquisition

Data were acquired using an Agilent 34970A (Keysight Technologies). Keysight VEE software was used to record the flow and temperature values. The readings were recorded when the system reached a steady-state condition at each tested flow rate value. The steady-state condition was assumed to have been achieved when the fluctuations for the thermocouples were less than 0.04 °C. This usually required a time of approximately 35 min for higher flow rates and 1 h for lower flow rates. All the data, which were logged for 5 min at 3 s intervals, were averaged to obtain a single set of data for further calculations. The average values were used as an input to verify the numerical model.

The heat dissipated by the heater was manually adjusted by the DC power supply. The test was conducted under two different heat fluxes of 15 $\mathrm{kW\,m^{-2}}$ and 30 $\mathrm{kW\,m^{-2}}$ based on the planform area $A_{planform}(= 48.4 \times 140\,\mathrm{mm^2})$. The flow rate changed from 14.7 $\mathrm{kg\,h^{-1}}$ to 120.2 $\mathrm{kg\,h^{-1}}$, which corresponds to a Reynolds number ranging from 170 to 1,380.

The imposed electrical power by DC unit can be calculated as:

$$E = V.I \tag{1}$$

where V is the voltage in (V) and I is a current in (A).

The steady-state sensible heat gain by the working fluid can be expressed as follows:

$$\dot{Q}_{sensible} = \dot{m}\, c_p\, (T_{blk,out} - T_{blk,in}) \tag{2}$$

where $\dot{m}$ was measured with the Coriolis mass flow meter. The gear pump assured a constant water flow rate for each test condition. The Coriolis mass flow meter measured the density in addition to the mass flow rate. The measured density values were compared with the obtained polynomial regression based on the provided data [47]. The difference was found to be approximately 1%. Hence, thermal properties were assumed and calculated according to Table 3. Note that all of the thermal properties were read at the arithmetic mean fluid temperature. The working fluid bulk temperature was measured with the RTDs located upstream and downstream of the minichannel. The inlet water temperature was fixed at $25\,^{\circ}\mathrm{C}\,(\pm 0.15)$.
The imposed electrical power can be compared to the magnitude of absorbed heat by distilled water passing thorough the minichannel in order to calculate the heat loss from the system.

$$\dot{Q}_{loss} = E - \dot{Q}_{sensible} \tag{3}$$

The heat loss to the atmosphere was determined to be no more than 8% of the added power input for all of the investigated cases. For instance, more than 97 W out of the input power of 103 W was absorbed by the working fluid at a low Reynolds number of 170. In contrast, 101 W out of 103 W was absorbed at the highest Reynolds number ($Re \approx 1,380$). The effective heat flux was calculated based on the top planform area of the HX, as follows:

$$q'' = \frac{\dot{m}\, c_p\, (T_{blk,out} - T_{blk,in})}{A_{HX_{Planform}}} \tag{4}$$

Because the direct measurement of the HX's inner-wall temperature was not

feasible, a 1D conduction formulation was applied, as described below:

$$T_{wall} = T_{measured} - (\frac{s\,q''}{k_{solid}}) \tag{5}$$

where s is the distance between the measured surface temperature and the inner-channel wall. This method was applied successfully by other researchers, including Lee et al. [10] and Zeng et al. [48]. The average convective heat transfer coefficient was:

$$\bar{h} = \frac{\dot{Q}_{sensible}}{NA_{wetted}(\overline{T}_{wall} - \overline{T}_{fluid})} \tag{6}$$

where N is the number of channels, and A_{wetted} is the wetted area, which equals $2L(a+b)$ in the case of a smooth channel. The surface areas of the VGs were added for the channel equipped with VGs. $\overline{T}_{wall}$ is the average of the surface temperature along the channel, and $\overline{T}_{fluid}$ is the mean fluid temperature. Finally, the Nusselt number was calculated using the following equation:

$$\overline{Nu} = (\frac{\bar{h}D_h}{k_{fluid}}) \tag{7}$$

It should be mentioned that the experiment was repeated with a lower heat flux after a month under the same conditions. There was an excellent agreement, which indicates the repeatability of the data.

4. Uncertainty Analysis

4.1. Calibration of thermocouples

For mini/microchannel heat sinks or HXs, the temperature difference between the fluid bulk and the wall temperature is typically rather small, particularly at high flow rates, due to the high thermal performance of these components. Low temperature differences usually result in large uncertainties in the thermal performance evaluation of HXs. Hence, a further temperature calibration was required to reduce the associated uncertainty. For this purpose, a liquid bath (Isotech Hyperion Site) and a RTD (Fluke 1551a) with an accuracy of 0.05 °C were used. The liquid bath helped to maintain a constant fluid temperature by stirring the fluid. The bath was filled with distilled water and it was insulated with Armaflex insulation material to reduce the environmental disturbance. The thermocouples were tied to the bodies of the RTDs with zip ties, and the thermocouple junctions were connected to the data acquisition system. Thermocouples were inserted inside the liquid bath from the top side through very narrow holes in the insulation material. Note that the levels of the thermocouple tips were perfectly aligned with the RTD to measure the same spot inside the bath. The liquid bath temperature was set to 20 °C, and it was left for 1 h to reach the steady-state condition. Subsequently, temperature readings were logged every 3 s for 3 min. The procedure explained above was repeated for every 5 °C until the temperature reached 40 °C. A linear curve fit of each thermocouple was obtained considering the temperature of the Fluke RTD as the true value. This method was advantageous since it considers the errors in reference box, the extension cable, and the data acquisition. Finally, the reliability of the

obtained equation was verified by correcting the thermocouple readings at different liquid bath temperatures. There was an excellent agreement with the RTD readings by performing this methodology.

4.2. Error analysis

In general, experimentally obtained measurements and values deviate from the true values because of the intrinsic errors associated with the experiment. These errors can be attributed to instruments, facilities, human factors, and environmental disturbance. Therefore, knowledge of such experimental uncertainties is crucial in the validation and calibration of computer simulations [49]. An experiment can be deemed truly complete only if the results are analyzed in light of these uncertainties.

Vernier caliper was used to measure the width a and height b of minichannel prior to conducting the experiments. A maximum deviation of 9% for the hydraulic diameter with respect to the nominal design value was found. After performing the experiments, the channels were cut from the top plane and the uniformity of the dimensions along the channel length was examined. The variations of the channel's width a after cutting was found to be within $\pm 2\%$ of the channel width at the inlet and the outlet. For the uncertainty calculation associated with the average heat transfer coefficient, the uncertainty of the VGs surface area were also taken into account using scanning electron microscopy (SEM) images, see Fig. 7. Due to the high number of embedded VGs inside each test section, uncertainty of the other VGs assumed to be the same as of the ones obtained through SEM images.

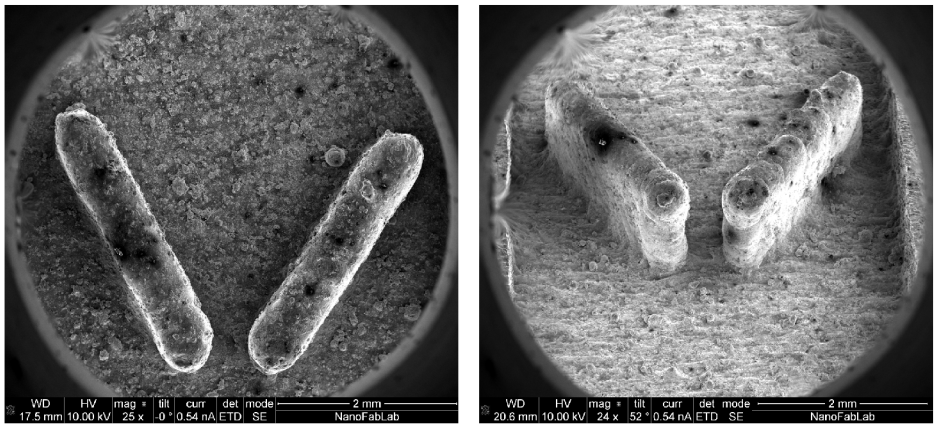
WD HV mag tilt curr det mode
17.5 mm 10.00 kV 25 x -0 ° 0.54 nA ETD SE
2 mm
NanoFabLab
WD HV mag tilt curr det mode
20.6 mm 10.00 kV 24 x 52 ° 0.54 nA ETD SE
2 mm
NanoFabLab

(a)

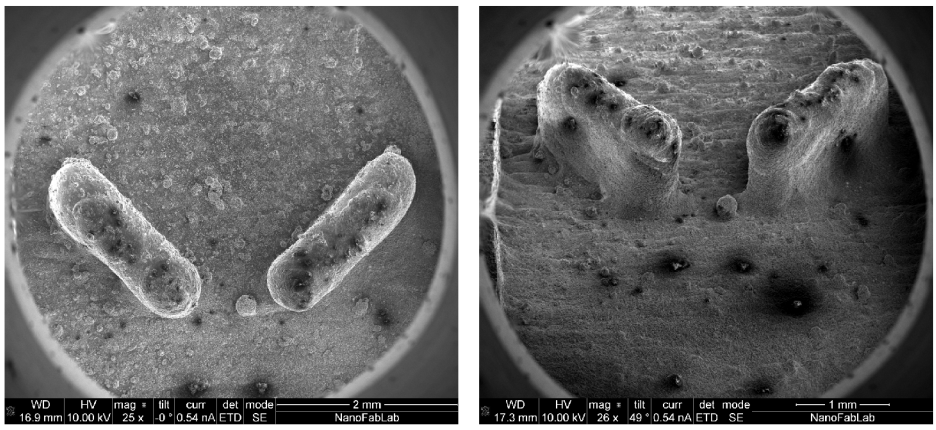
WD HV mag tilt curr det mode
16.9 mm 10.00 kV 25 x -0 ° 0.54 nA ETD SE
2 mm
NanoFabLab
WD HV mag tilt curr det mode
17.3 mm 10.00 kV 26 x 49 ° 0.54 nA ETD SE
1 mm
NanoFabLab

(b)

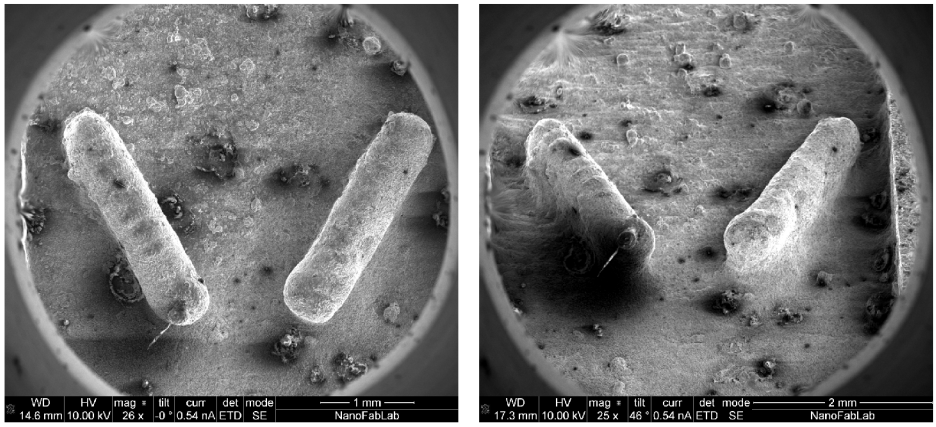

(c)

Figure 7: SEM analysis of each tested prototypes: (a) Prototype 2 ($l = 3\,\text{mm}$, $\beta = 30°$, $H = 1.2\,\text{mm}$, $S = 18\,\text{mm}$). (b) Prototype 3 ($l = 2\,\text{mm}$, $\beta = 45°$, $H = 1.2\,\text{mm}$, $S = 17\,\text{mm}$). (c) Prototype 4 ($l = 2.5\,\text{mm}$, $\beta = 30°$, $H = 0.8\,\text{mm}$, $S = 22.5\,\text{mm}$)

In this study, the uncertainty analysis was based on the root sum square method described by Moffat [50] and the ASME standard [51]. Accordingly, the uncertainty associated with the Reynolds number and average heat transfer coefficient could be expressed as following:

$$U_{Re} = \pm\sqrt{(\frac{\partial Re}{\partial \rho}U_\rho)^2 + (\frac{\partial Re}{\partial u_m}U_{u_m})^2 + (\frac{\partial Re}{\partial D_h}U_{D_h})^2 + (\frac{\partial Re}{\partial \mu}U_\mu)^2} \tag{8}$$

$$U_{\bar{h}} = \pm\sqrt{(\frac{\partial \bar{h}}{\partial \dot{Q}}U_{\dot{Q}})^2 + (\frac{\partial \bar{h}}{\partial A_{conv}}U_{A_{conv}})^2 + (\frac{\partial \bar{h}}{\partial T_{wall}}U_{T_{wall}})^2 + (\frac{\partial \bar{h}}{\partial T_{fluid}}U_{T_{fluid}})^2} \tag{9}$$

Table 2 lists the measuring tools that have been used during this study and their corresponding accuracies. The uncertainties in the derived parame-

ters of the channel with the highest uncertainty are also listed (e.g prototype 2). Using Engineering Equation Solver (EES) software, the analysis showed that the expanded uncertainty (95% confidence interval) of the convective heat transfer coefficient for the prototype 2 ranged from 9.0% to 47.4% depending on the flow rate (Table 2). As the flow rate increased, the temperature difference between the inlet and the outlet decreased, leading to higher uncertainties. The main source of error in the analysis was the temperature measurements of both the minichannel surface and the working fluid.

Table 2: Experimental tools accuracy information and uncertainty of derived parameters .

Experimental sensors	Affected parameters	Accuracy
Thermocouple (Omega, T-type)	T_{wall}	0.50 °C
RTD (Pentronic, 1/10 DIN)	$T_{blk,in}, T_{blk,out}$	0.04 °C at 20 °C
Coriolis mass flow meter (Micro Motion CMFS015M)	$\dot{m}$	±0.10% of rate (Liquid)
Turbine flow meter (Omega-FLR1012ST)	$\dot{V}$	±1.00% Full Scale

Variables	Range	Expanded uncertainty,%
h [$\mathrm{W\,m^{-2}K^{-1}}$]	1,645.4- 5,918.8	9.0- 47.4
Re [-]	169.5- 1,371.9	6.5- 7.3

5. Numerical Analysis

5.1. Computational model description

Since the experimentally tested prototypes have repetitive geometries, a single-channel unit, including half of the side solid wall ($t/2$), was chosen as the computational domain for each HX. The selected model assumed that the working fluid was distributed evenly between the channels, which helped to reduce the computational time. Figure 8 displays the chosen numerical model, the coordinate system, and the related dimensions. The dimensions of the VGs for the numerical simulations were consistent with the designed

prototypes and are in line with the details listed in Table 1. As demonstrated in Fig. 8, the inlet and outlet of the core computational part (i.e., the minichannel HX) were extended by 20 mm. The added extension, hereinafter called the fluid block, improved the computational convergence by ensuring no flow recirculation at the exit.

Another numerical modeling approach (not reflected in this study) involves cutting the single-channel unit mentioned above into half at the mid-plane. This would be advantageous in regard to the computational time, and for parametric and optimization studies that intend to compare the various design parameters. However, as the vortices were generated, there would be a strong span-wise velocity and temperature gradient within the fluid. This would be damped by this model technique; thus, inducing large numerical errors when comparing the results to the experiment. Therefore, the first modeling approach was used in the analysis.

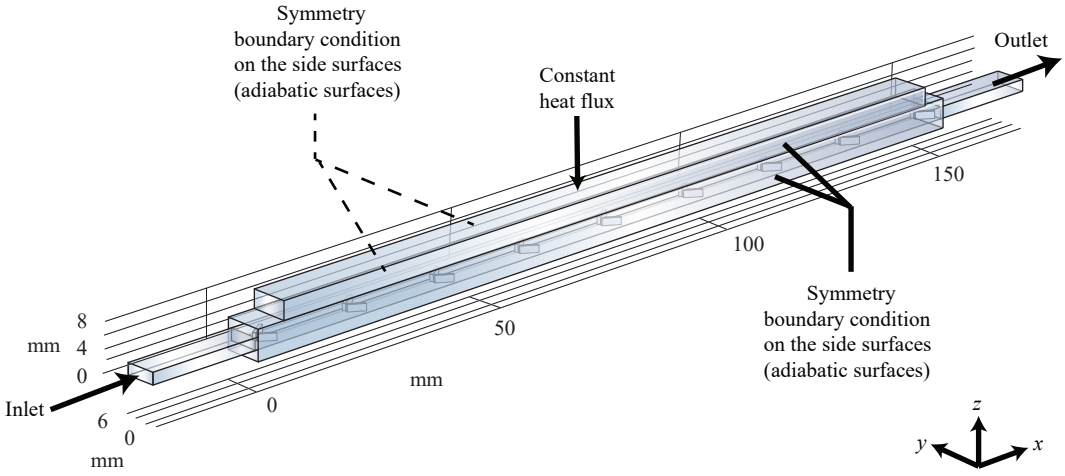

Figure 8: Computational domain and boundary conditions.

5.2. Governing equations and numerical data reduction

Several numerical and experimental studies of embedded VGs inside the mini/microchannel components showed that the flow could be safely considered to be laminar when the Reynolds number was below 1,700 although many vortices could be generated within the domain [52–55]. In addition, the experimental results of this study (presented in Section 6) showed no indication of transitional or turbulent flow within the tested flow range ($170 < Re < 1,380$) for the prototypes. Finally, It was determined that the use of the SST-kω turbulence model in combination with the Reynolds-averaged Navier-Stokes (RANS) equations yielded a near-laminar flow solution at a low-flow Reynolds numbers [56]. Thus, extra simulations based on the SST-kω turbulent model and the highest tested flow range ($Re \approx 1,380$) were conducted for the prototypes and were compared with the laminar flow solution. The maximum difference in the Nusselt number was determined to be less than 3%. As a result, the laminar flow model was considered for further numerical calculations.

The following assumptions were made to simplify the numerical simulation:

(1) The flow considered was to be steady-state, single-phase, laminar, and weakly compressible.

(2) The thermal properties of the working fluid varied with the temperature and were based on Table 3. For the solid domain, the properties were constant and in agreement with the obtained material properties for the AlSi10Mg alloy.

(3) The effect of viscous dissipation could be safely neglected because of the

designed channel size, the choice of the working fluid, and the investigated flow range [57, 58].

(4) The influence of gravity and radiation heat transfer were neglected.

Under the above assumptions, the governing equations were as follows:

- Continuity:

$$\nabla \cdot (\rho \vec{V}) = 0 \tag{10}$$

- Conservation of momentum:

$$\rho(\vec{V} \cdot \nabla)\vec{V} = -\nabla p + \mu \nabla^2 \vec{V} \tag{11}$$

- Conservation of energy:

$$\vec{V} \cdot \nabla T = \nabla \cdot (\frac{k}{\rho c_p} \nabla T) \tag{12}$$

The governing equations within the solid domain were transformed as follows:

- Conservation of momentum:

$$\vec{V} = \vec{0} \tag{13}$$

- Conservation of energy:

$$\nabla^2 T = 0 \tag{14}$$

Note that the temperature of the working fluid at the minichannel outlet was calculated as the mass-weighted temperature. The minichannel wall

temperature was calculated as the line average of the inner surface to ensure consistency with the experimental conditions (i.e., corrected thermocouple readings).

The pressure drop was defined as the difference in the static pressure between the inlet and outlet:

$$\Delta P = (\overline{P}_{in} - \overline{P}_{out}) \tag{15}$$

A nondimensional form of the pressure drop is the apparent friction factor f_{app}, expressed as [42]:

$$f_{app} = \frac{\Delta P D_h}{2\rho u_m^2 L} \tag{16}$$

Where ΔP is the pressure drop through the channel, u_m is the mean fluid velocity, and L is channel's length.

Finally, in order to compare the performance of the enhanced heat exchanger surface with that of the smooth channel surface case, the global performance evaluation criteria (PEC) at constant pumping power was used [59–61]:

$$PEC = \frac{\frac{Nu}{Nu_s}}{(\frac{f_{app}}{f_{app,s}})^{\frac{1}{3}}} \tag{17}$$

The nominator of each fraction belongs to the enhanced surfaces while the denominator having subscript (s) represent the smooth surface.

Table 3: Thermo-physical properties of AlSi10Mg and distilled-water. The unit of temperature is Kelvin.

Thermal property	AlSi10Mg [46]	Distilled water [47]
$\mu\,[\mathrm{kg\,m^{-1}\,s^{-1}}]$	-	$(3.82937\mathrm{E}{-11})T^4 - (5.19160\mathrm{E}{-8})T^3 + (2.64389\mathrm{E}{-5})T^2 - (6.00086\mathrm{E}{-3})T + (5.13161\mathrm{E}{-1})$
$c_p\,[\mathrm{J\,kg^{-1}\,K^{-1}}]$	846	$(3.04565\mathrm{E}{-6})T^4 - (4.03634\mathrm{E}{-3})T^3 + (2.01262)T^2 - (4.47105\mathrm{E}2)T + (4.14867\mathrm{E}4)$
$k\,[\mathrm{W\,m^{-1}\,K^{-1}}]$	110.93	$(2.18062\mathrm{E}{-8})T^3 - (2.93359\mathrm{E}{-5})T^2 + (1.32323\mathrm{E}{-2})T - 1.30788$
$\rho\,[\mathrm{kg\,m^{-3}}]$	2620.73	$(1.69701\mathrm{E}{-5})T^3 - (1.99752\mathrm{E}{-2})T^2 + (7.13761)T + (1.94866\mathrm{E}2)$

5.3. Boundary conditions

The commercial software package Comsol Multiphysics v5.3a, which solves governing equations based on the FEM, was used as the numerical tool. The conjugate heat transfers and laminar model were considered since they best represented the experiment. Referencing Fig. 8, the mass flow rate and a uniform temperature were applied to the inlet of the fluid block according to the experimental input. At the fluid block outlet, an outlet boundary condition, with a relative pressure of 0 Pa, and an outflow boundary condition were assumed for the laminar flow and heat transfer modules, respectively. An adiabatic boundary condition was chosen for the other surfaces of the fluid blocks. Finally, no-slip boundary conditions were considered for the fluid walls. For the solid domain, a uniform heat flux was applied to the top of the minichannel surface, which is consistent with the experimental results. Symmetry boundary conditions were applied to the sidewalls.

5.4. Method validation, grid sensitivity, and solver settings

The ability of the selected FEM-based software to produce accurate results for the conjugate heat transfer and the laminar model was previously verified by the present authors [44]. In the aforementioned study, the results of numerical predictions were compared with classical correlations for a circular tube, assuming constant wall temperature, as well as with the experiment of Liu et al. [30], and good agreement was achieved. In this paper, a tetrahedral element was applied to the VGs and the planform area while non-uniform tetrahedral elements were used for discretizing the other domains. Finer resolutions were used near the walls and the VGs. The grid sensitivity was conducted for each prototype at the highest tested mass flow rate separately and only a summarized conclusion is given for prototype 3 as presented in Fig. 9. As shown, Mesh 3 and Mesh 4 differed by less than 1.15% for the average Nusselt number. Therefore, considering the computational accuracy–time tradeoff, Mesh 3 (with 1,069,783 elements) was selected for the analysis. The temperature field was represented using a quadratic element, whereas velocity and pressure were represented as second- and first-order discretizations (P2+P1), respectively. P2+P1 uses quadratic interpolation of the velocity field and linear interpolation of the pressure field. The conservation equations were solved using a segregated approach and a direct solver (PARDISO). In the convergence criteria analysis, the simulations were considered to have converged when the relative tolerance was less than 5×10^{-5} for the continuity, momentum, and energy equations.

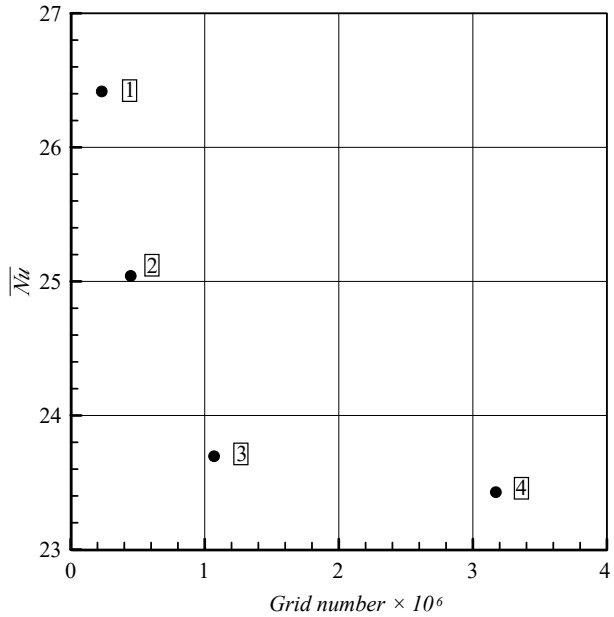

Figure 9: Mesh independence study for Prototype 3 ($l = 2\,\text{mm}$, $\beta = 45°$, $H = 1.2\,\text{mm}$, $S = 17\,\text{mm}$) and $Re = 1,366$.

6. Results

6.1. Heat transfer

For the smooth channel, the experimental single-phase heat transfer data were measured and compared against well-known correlations and a numerical simulation. Thermal entry region correlations were considered for comparison purposes. This is because for most of the experimental conditions, the flow was thermally developing through a large portion of the channel's length ($0.006 < x^* \equiv L(D_h RePr)^{-1} < 0.053$). The only case where the flow was fully developed at the outlet was the lowest tested flow rate ($Re \approx 176$). Among the classical correlations, the results were compared with the modified Hausen formula [41]. The Hausen correlation was originally developed for a circular tube with a constant wall temperature boundary condition as

described in Eq. 18.

$$\overline{Nu} = 3.66 + \frac{0.0668 Gz_D}{1 + 0.04 Gz_D^{2/3}}, \quad T_{\text{surface}} = \text{constant} \tag{18}$$

where Gz_D is the Graetz number ($Gz_D \equiv D_h ReP rL^{-1}$). However, by looking closer at Eq. 18, it can be demonstrated that the constant in the equation represents the fully developed value in the laminar region. By changing the constant to the corresponding channel aspect ratio ($\alpha \approx 2.5$) and the constant heat flux boundary condition, this can lead to a modified formula. This can be written as follows:

$$\overline{Nu} = 4.46 + \frac{0.0668 Gz_D}{1 + 0.04 Gz_D^{2/3}}, \quad \text{q}''_{\text{surface}} = \text{constant}, \ \alpha = 2.5 \tag{19}$$

Another correlation used in the analysis is the one recently presented by Lee and Garimella [62] for thermally developing flow based on the numerical simulations. Using the finite volume method, they showed that the results of the conjugate heat transfer approached that the constant axial heat rate with a constant temperature around the tube periphery (known as the H1 boundary condition) for minitube/microtube materials with high thermal conductivity. Based on the numerical simulation, the correlation for the average Nusselt number can be expressed as follows:

$$\overline{Nu} = \frac{1}{C_1 (x^*)^{C_2} + C_3} + C_4, \ for \ 1 \leq \alpha \leq 10 \tag{20}$$

where

C_1 =$(-2.757\text{E}{-3})\alpha^3 + (3.274\text{E}{-2})\alpha^2 - (7.464\text{E}{-5})\alpha + 4.476$

C_2 =6.391E−1

C_3 =$(1.604\text{E}{-4})\alpha^2 - (2.622\text{E}{-3})\alpha + (2.568\text{E}{-2})$, and

C_4 =$7.301 - (1.311\text{E}1)\alpha^{-1} + (1.519\text{E}1)\alpha^{-2} - 6.094\alpha^{-3}$

It is interesting to note that the results of the average Nusselt number obtained from the modified Hausen formula deviated less than 3.1% from the correlation developed by Lee and Garimella [62] within the studied range.

The experimental results were also compared with the modified Baehr-Stephan [63] and Sieder-Tate [64] equations. These correlations were developed for the simultaneously developing flow (Eq. (21-22)).

$$\overline{Nu} = \frac{\frac{4.46}{\tanh[2.264 Gz_D^{-1/3} + 1.7 Gz_D^{-2/3}]} + 0.0499\, Gz_D \tanh(Gz_D^{-1})}{\tanh(2.432\, Pr^{1/6} Gz_D^{-1/6})} \tag{21}$$

and:

$$Nu = 1.86\, Gz_D^{1/3} \tag{22}$$

Note that the constant in Eq. 21 was modified according to the constant heat flux boundary condition and the aspect ratio of the channel ($\alpha \approx 2.5$). Figure 10 illustrates the comparison between the experimental results of the smooth channel with the specified correlations and the numerical solution. The corresponding value of the fully developed flow is also presented. Figure

10 indicates that the experimental results had a good agreement with the numerical solution. Furthermore, among the correlations, the modified Hausen and Lee and Garimella equations developed for thermally developing flow predicted the average Nusselt number more accurately than the simultaneously developing correlations (i.e. modified Baehr-Stephan [63] and Sieder-Tate [64]). In fact, 79% and 95% of the obtained experimental data points were within ± 10% of the thermally developing correlations (modified Hausen [41], and Lee and Garimella [62]) and the numerical simulations, respectively.

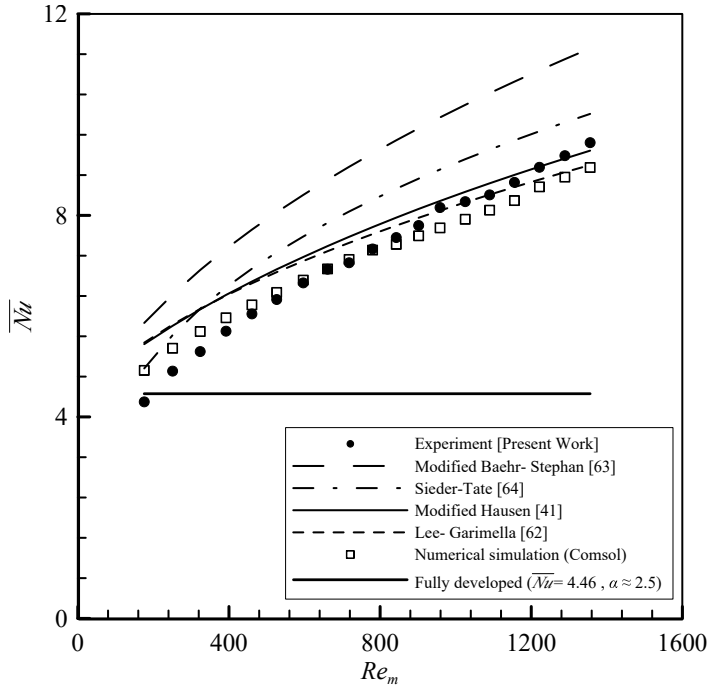

Figure 10: Comparison of the smooth channel experimental average Nusselt number with the correlations and numerical simulation.

The results of the heat transfer for the different prototypes are shown in Fig. 11 (a-d). To ensure the repeatability of the measured values, the experiment related to each prototype was repeated in the case of a lower heat

flux after a month. There was also a very good agreement, which confirms the repeatability of the experiment. A comparison was made with the simulation in the case of a lower heat flux and the repeated measurement.

Figure 12 displays a comparative summary of the experimental heat transfer results for all of the prototypes.

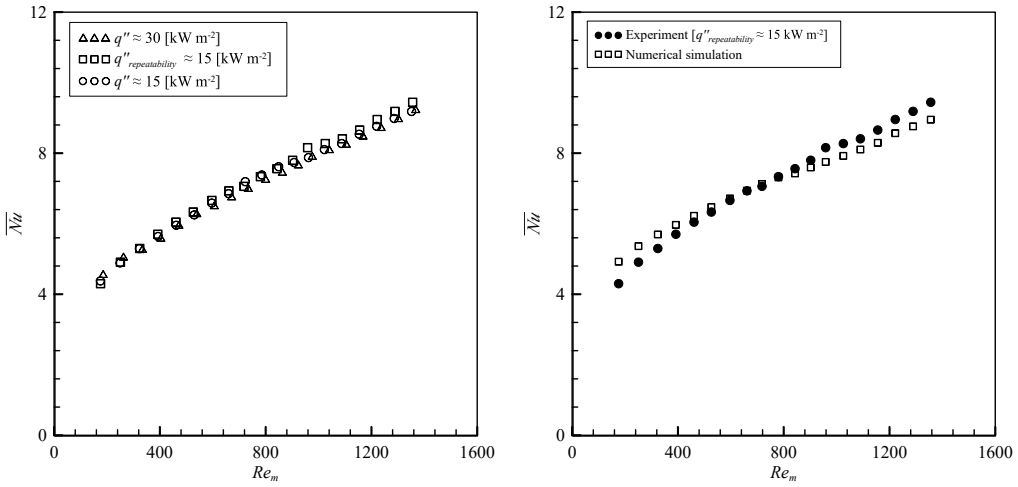

(a)

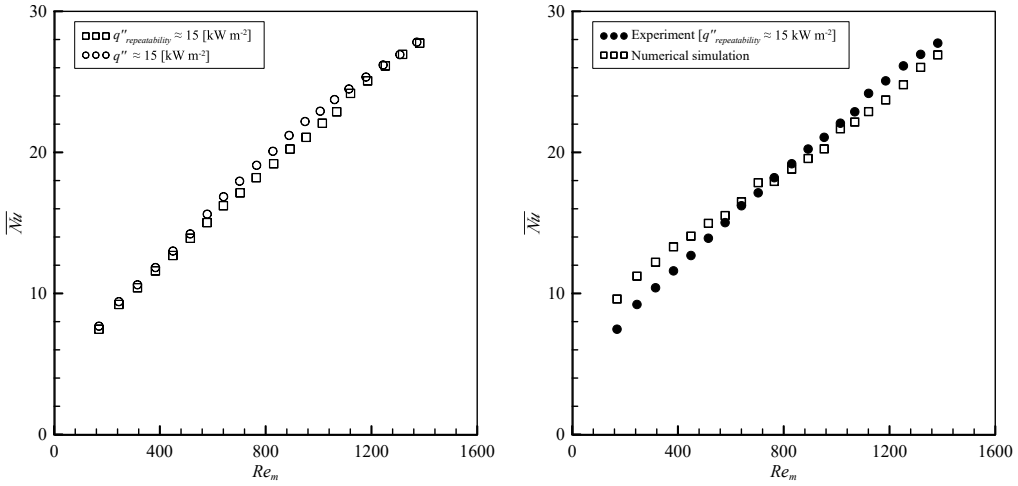

(b)

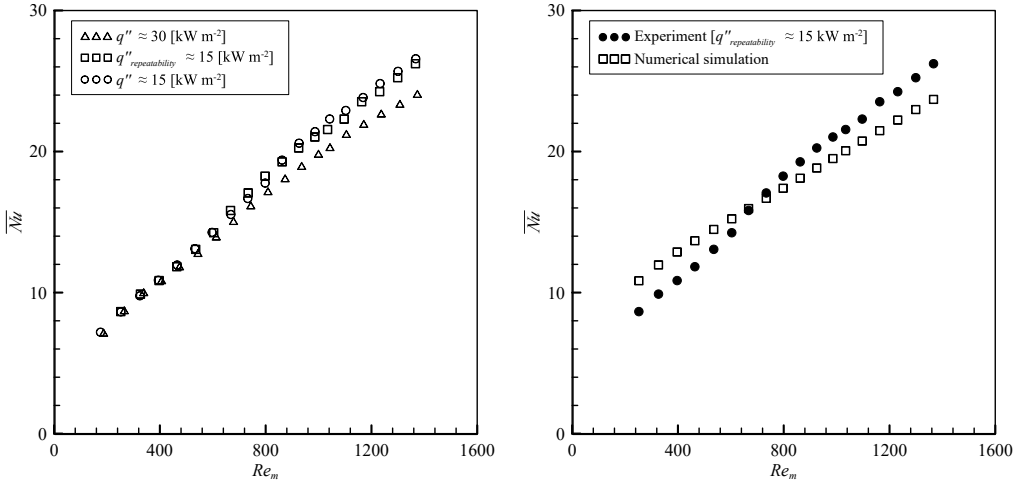

(c)

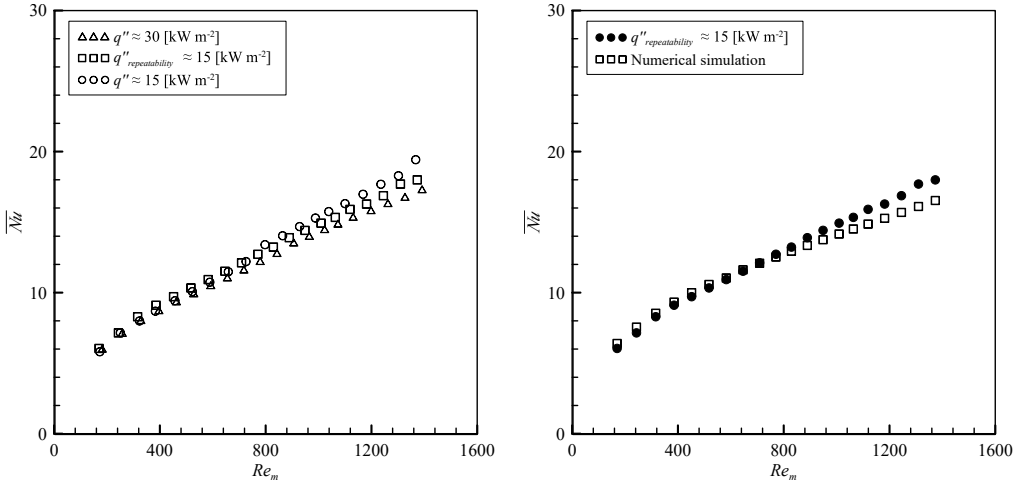

(d)

Figure 11: Experimental and numerical results of average Nusselt number as a function of Reynolds number for different tested prototypes. (a) Prototype 1 (smooth channel). (b) Prototype 2 ($l = 3\,\text{mm}$, $\beta = 30°$, $H = 1.2\,\text{mm}$, $S = 18\,\text{mm}$). (c) Prototype 3 ($l = 2\,\text{mm}$, $\beta = 45°$, $H = 1.2\,\text{mm}$, $S = 17\,\text{mm}$). (d) Prototype 4 ($l = 2.5\,\text{mm}$, $\beta = 30°$, $H = 0.8\,\text{mm}$, $S = 22.5\,\text{mm}$)

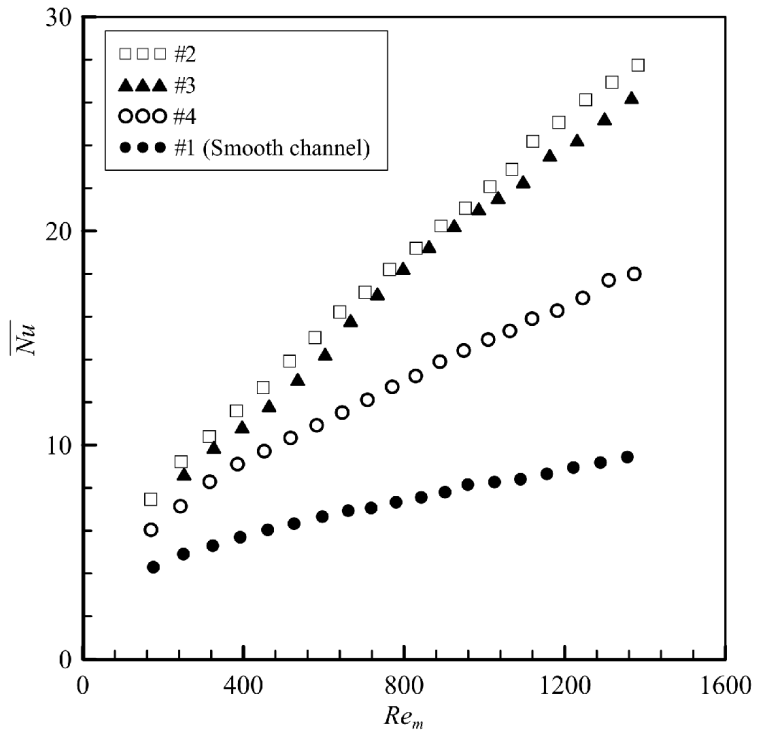

Figure 12: Comparison of the experimental average Nusselt number as a function of Reynolds number for different test sections at lower heat flux ($q''_{repeatability} \approx 15\ \mathrm{kW\,m^{-2}}$).

As indicated, the use of VGs considerably enhances the thermal exchange. Prototypes 2 and 3 show a superior convective heat transfer in comparison to prototypes 1 (smooth channel) and 4. For example, by having a Reynolds number of 175, the average Nusselt number of channel 2 is 71% higher than the smooth channel. At the highest tested flow rate ($Re \approx$ 1,380), the average Nusselt number of channel 2 was approximately three times more than the smooth channel. The convective heat transfer increased as the Reynolds number increased mainly due to the generation of stronger longitudinal vortices. The use of a higher length, higher height, and a higher angle of attack dramatically impacted the heat transfer rate. In addition, embedding a pair of VGs near each other (i.e. a lower longitudinal pitch S) maintained the strength of the vortices throughout the channel; thus, increasing the flow mixing and convection. As reflected in Fig. 11, the numerical tool predicted the experimental results reasonably well. Considering that the numerical results followed the same trend as the experiment with the values within the experimental uncertainties, the numerical results were determined to be trustworthy. Therefore, the flow and heat transfer characteristics can be further investigated by performing simulations.

6.2. Pressure drop and performance evaluation criteria

The numerical pressure drop and the friction factor results for the smooth and the enhanced prototypes are illustrated in Figs. 13. As the Reynolds number increases, the pressure drop and the friction factor increases and decreases, respectively. At the highest tested Reynolds number ($Re \approx 1,380$), the pressure drop of the prototypes 2, 3 and 4 increased by a factor of 8.7, 7.9 and 2.7, respectively, as compared to the smooth channel. The considerably higher pressure drop across prototype 2 and 3 compared with prototype 4 was attributed to their choice of design parameters. The performance evaluation criteria (PEC) as a function of Re number is, also, shown in Fig. 14. As depicted, the PEC for the enhanced prototypes lies within 1.27 to 1.48 within the entire Reynolds range, except for the prototype 4 at the very low Reynolds number. An increasing trend for the prototype 2 is seen as function of Reynolds, pointing out to the superiority of the effect of the longer VGs length at higher Reynolds number.

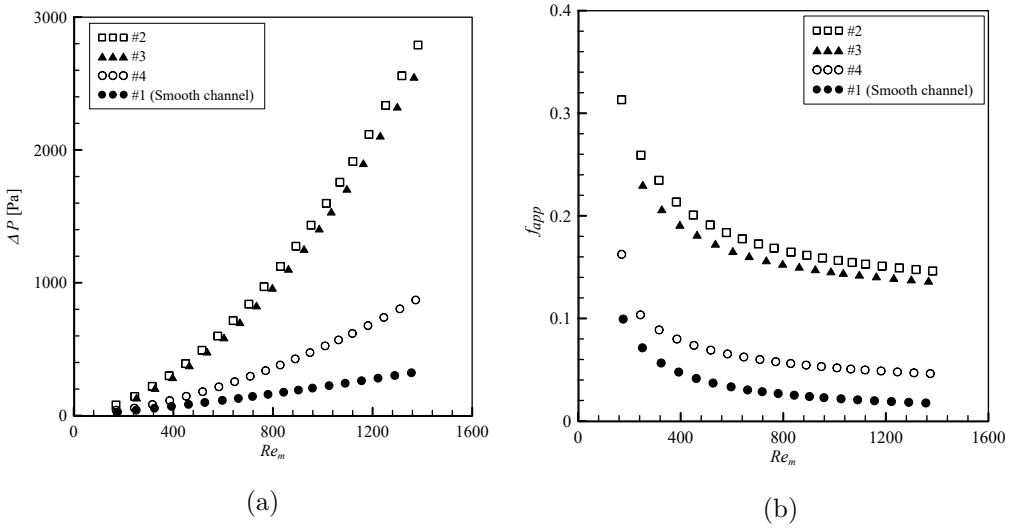

Figure 13: Comparison of numerical pressure drop and apparent friction factor as a function of Reynolds number for different test sections: (a) pressure drop, (b) apparent friction factor.

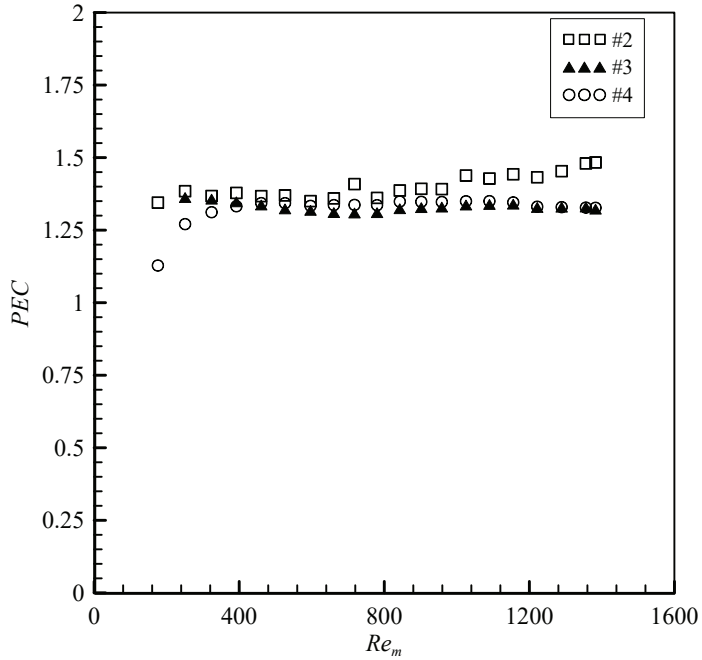

Figure 14: Performance evaluation criteria as a function of Reynolds number for different test sections.

6.3. Flow and thermal characteristics of the manufactured prototypes

In order to further investigate the thermal characteristics of each prototype, extra simulations were conducted for the inlet Reynolds numbers of 481 and 1,284. The constant heat flux of 50 $\mathrm{kW\,m^{-2}}$ was applied to the channel's top surface, and inlet temperature was fixed at 25 °C. Higher heat flux was considered in this set of simulations to get enough flow temperature differences between inlet and outlet, especially at high Reynolds number, facilitating the comparison of the thermal enhancement among the prototypes. The velocity and temperature contours, respectively, of a smooth channel at an inlet velocity of 0.15 $\mathrm{m\,s^{-1}}$ and $Re_{in} = 481$ at approximately 108 mm from the inlet are depicted in Figs. 15(a) and (c). "The velocity profile had the expected symmetric parabolic shape and the temperature near the solid–fluid interference was high. The flow at this distance from the inlet was hydrodynamically fully developed, but thermally developing, confirming that the velocity boundary layer grew faster than the thermal boundary layer for $Pr > 1$. As the thermal entry length increased with an increasing Re, the thermal boundary layer at a given position in the channel would be thicker with a low Re, and the heat transfer performance therefore lower (Figs. 15(c) and (d)). Considering that the axial velocity component was dominant, no cross-mixing occurred to promote heat transfer. In contrast, vortex generators can create complex flows that can significantly affect the overall and local heat transfer. The minichannel with VGs exhibited a very different flow (Fig. 15(b)). Here, the VG occupied a significant portion of the minitube cross-section. This caused the flow to accelerate over the VG and to generate 3D vortices on the backside of the VG. The vortices extended downstream

of the VGs caused high mixing, and an increased interaction between the channel walls and the flow core; thus, disturbing the boundary layer. Consequently, a thinner thermal boundary layer thickness was maintained along the channel length, thereby increasing the convection" [44].

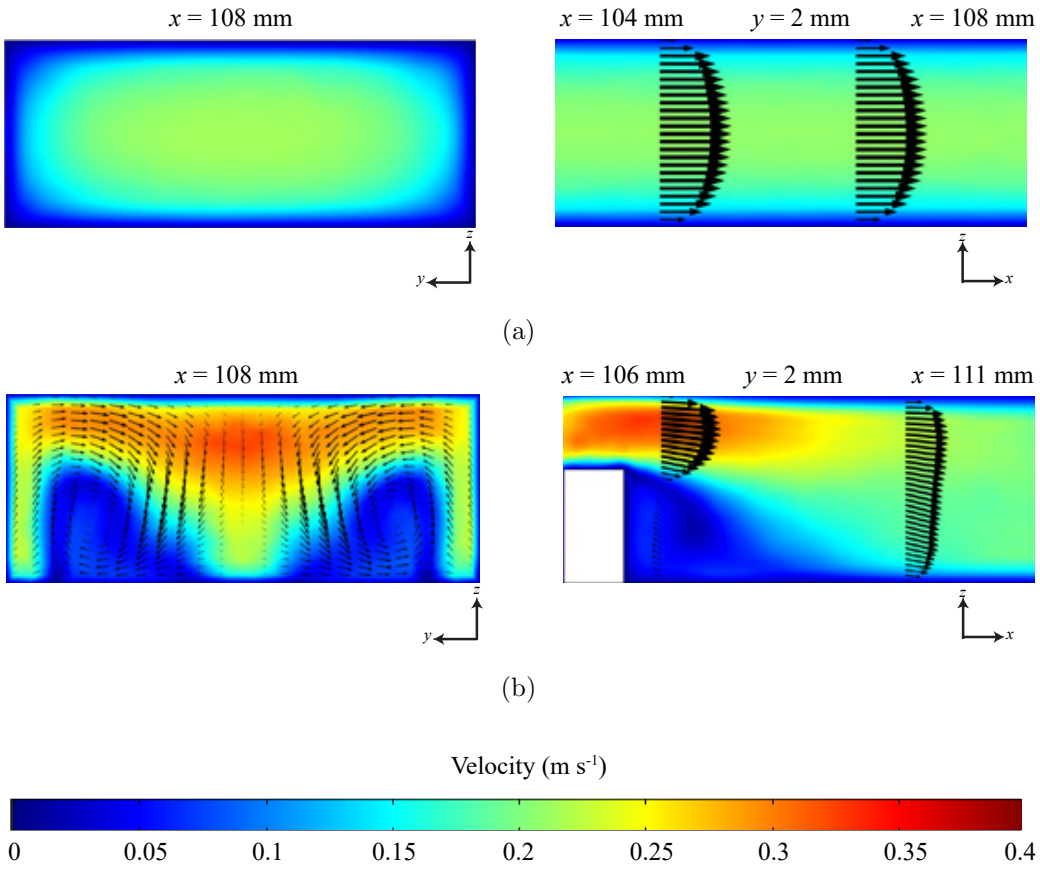

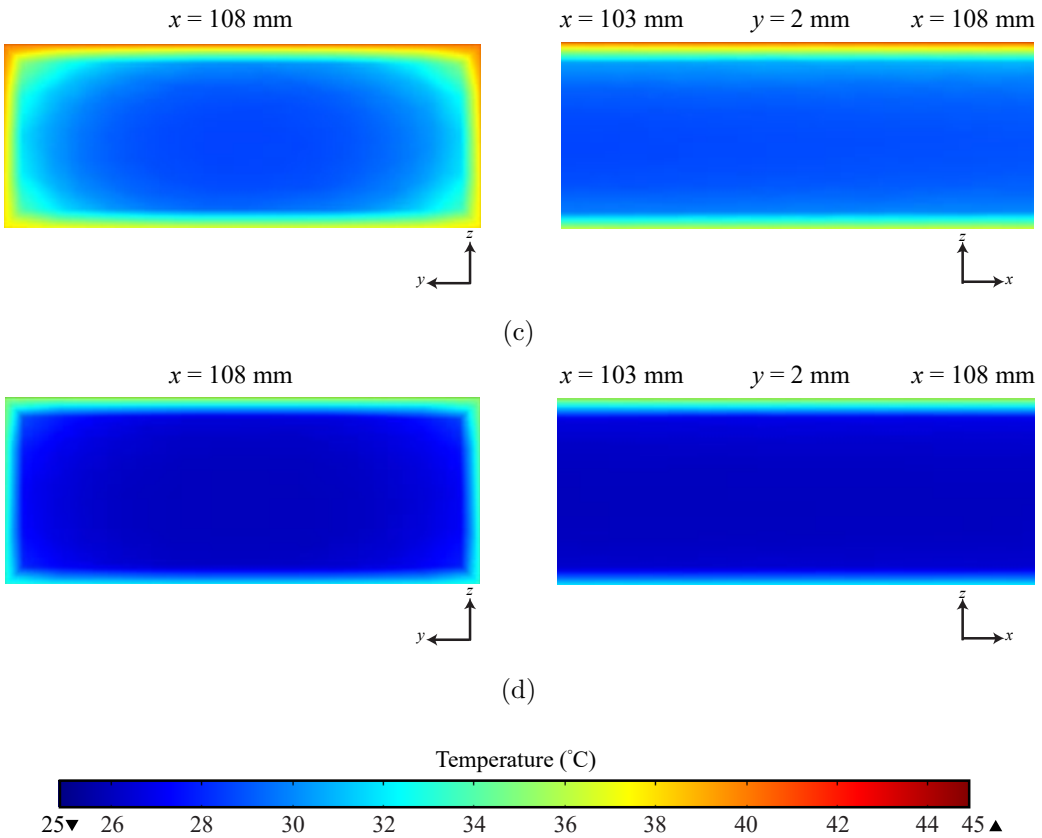

Figure 15: Minichannel velocity and temperature contours: (a) smooth channel, $u_{in} = 0.15\,\mathrm{m\,s^{-1}}$, $Re_{in} = 481$, (b) Prototype 3 equipped with VGs ($\beta = 45°$, $l = 2\,\mathrm{mm}$, $H = 1.2\,\mathrm{mm}$, $S = 17\,\mathrm{mm}$), $u_{in} = 0.15\,\mathrm{m\,s^{-1}}$, $Re_{in} = 481$, (c) smooth channel, $u_{in} = 0.15\,\mathrm{m\,s^{-1}}$, $Re_{in} = 481$, $103\,\mathrm{mm} < x < 108\,\mathrm{mm}$, (d) smooth channel, $u_{in} = 0.4\,\mathrm{m\,s^{-1}}$, $Re_{in} = 1,284$, $103\,\mathrm{mm} < x < 108\,\mathrm{mm}$.

Figures 16 and 17 illustrate the velocity and temperature profiles for the channels equipped with VGs at the cross-section parallel to the zy-plane (perpendicular to the flow direction) and right after the third VG for the investigated low and a high Reynolds number. The results of smooth channel are also brought for the comparison. The velocity profiles indicate that the high-velocity regions were formed at the channel's top and side walls and a

space between the VGs. The formation of high-velocity regions could be attributed to the narrowed channel cross-sectional area due to the presence of the VGs. The extent of the generated high-velocity zones depends on the VG design parameters such as the height H, length l, and the angle of attack β. As a result, the high-velocity regions for prototypes 2 and 3 are formed in comparison to prototype 4. In addition, the pressure difference between the two sides of the VGs caused the formation of a pair of counter-rotating vortices, which could be considered as a main enhancement mechanism. Longitudinal vortices pushed the boundary layer down and had a thinning effect; thereby helping a higher thermal exchange between the coolant and the HX's wall. As illustrated in the temperature contour (Fig. 16(d)), a pair of counter-rotating vortices brought the near-wall high-temperature fluid to the center of the vortices and this was mixed with the cold fluid; hence, leading to an increased thermal interaction. In addition, longitudinal vortices thinned the boundary layer at the bottom surface. The intensity of the generated vortices in the case of prototype 4 was lower than prototypes 2 and 3 due to the lower height of the VGs. Figure 16(d) shows that the generated vortices were formed near the side walls and at a low height. Thus, a thicker thermal boundary layer could be observed, resulting in a relatively lower thermal enhancement in comparison with the other channels equipped with VGs.

Visualizing the flow from the top view helps to understand the flow characteristics at the downstream of the VGs more thoroughly. Figures 18 and 19 show the velocity contours and the streamlines of the different prototypes in the xy-plane and at a distance of 0.3 mm from the bottom inner-channel surface. As demonstrated in the velocity contours, the generated wake in pro-

totype 3 was larger due to the higher angle of attack. In this prototype, in comparison to the other two prototypes embedded with the VGs, a marginal delay in the dissipation of the high-velocity flow at the VG passage to the channel cross-sectional area in the form of longitudinal vortices can be seen.

In the wake regions, regardless of the Reynolds numbers, a pair of transverse vortices were generated in the xy-plane and they were perpendicular to the flow direction for the prototypes, which is reflected in the streamlines. In the case of the lower angle of attack of 30°, prototypes 2 and 4, small transverse vortices were generated in the proximity of the winglets; thus, allowing a quick formation of the longitudinal vortices (Figs. 18(a) and (c) and Figs. 19(a) and (c)). In contrast, at the higher angle of attack of 45°, larger transverse vortices were formed. This occupied a larger area and it disturbed the emergence of the dominant flow mechanism of the longitudinal vortices (Fig. 18(b) and Fig. 19(b)). The transverse vortices mixed the fluid locally in those small regions. While the transverse vortices could be influential in improving the local heat transfer, they decreased the relative effective length of the longitudinal vortices.

The thermal performances of the enhanced prototypes with respect to the benchmark prototype for the entire length of the channels are visualized in Figs. 20 and 21, and this applies for Reynolds numbers of 481 and 1,284, respectively. The formation of the thin thermal boundary layer throughout the entire channel length is indicated for the enhanced prototypes, which increased the convective heat transfer continuously along the channel length. The mean thermal performance superiority of prototypes 2 and 3, in comparison to prototype 4, is clearly understood by noticing the lower temperatures

of their VGs at the end of the channel and, correspondingly, the higher coolant temperature.

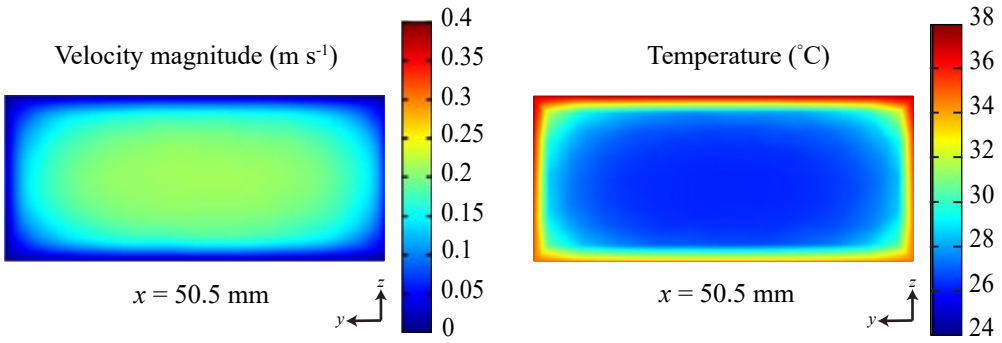

(a)

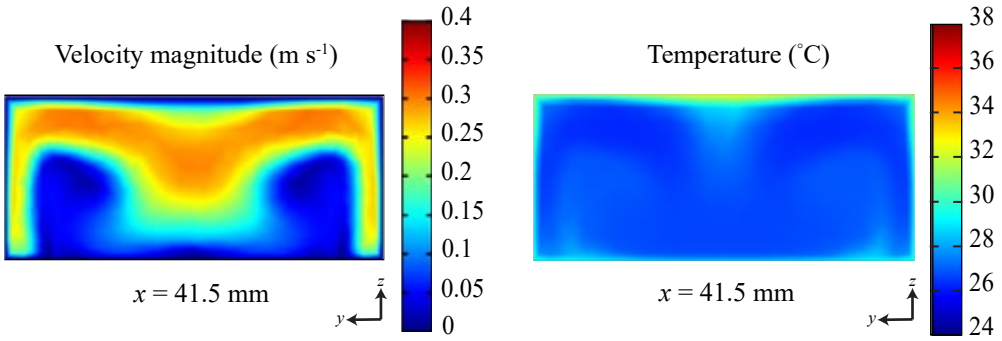

(b)

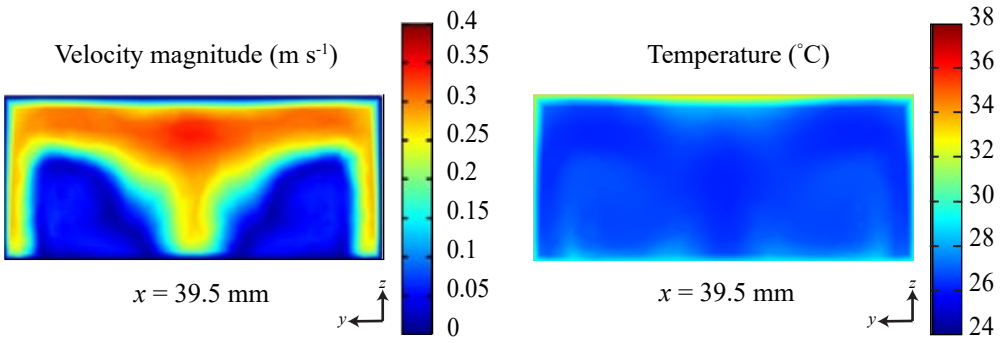

(c)

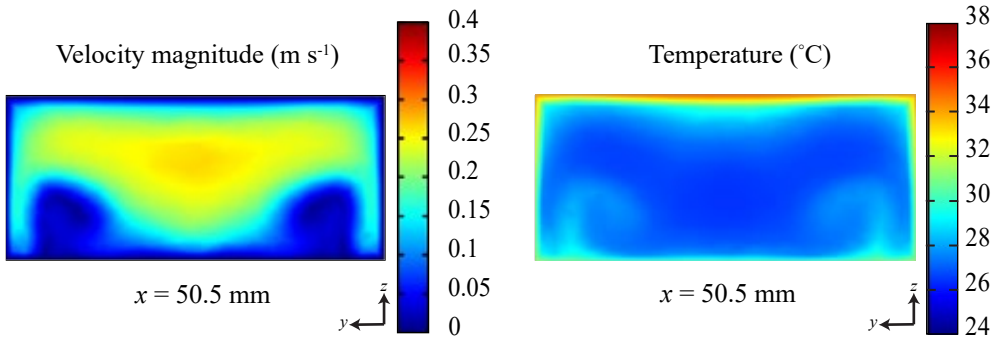

(d)

Figure 16: Velocity and temperature contours at $Re_{in} = 481$ (a) Prototype 1 (smooth channel). (b) Prototype 2 ($l = 3\,\text{mm}$, $\beta = 30°$, $H = 1.2\,\text{mm}$, $S = 18\,\text{mm}$). (c) Prototype 3 ($l = 2\,\text{mm}$, $\beta = 45°$, $H = 1.2\,\text{mm}$, $S = 17\,\text{mm}$). (d) Prototype 4 ($l = 2.5\,\text{mm}$, $\beta = 30°$, $H = 0.8\,\text{mm}$, $S = 22.5\,\text{mm}$)

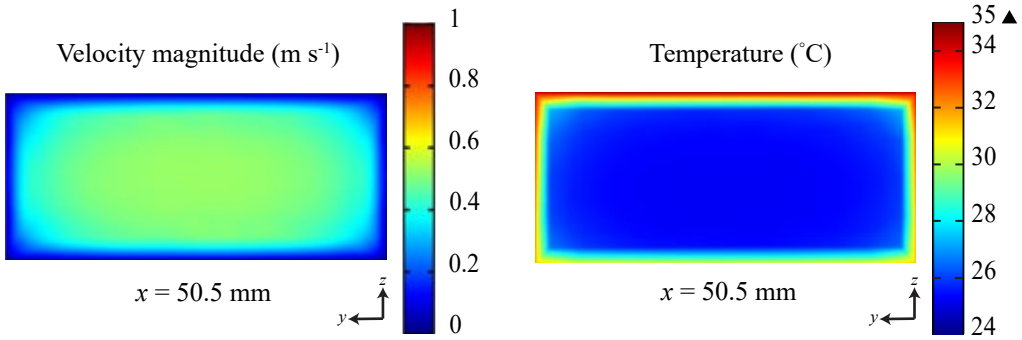

(a)

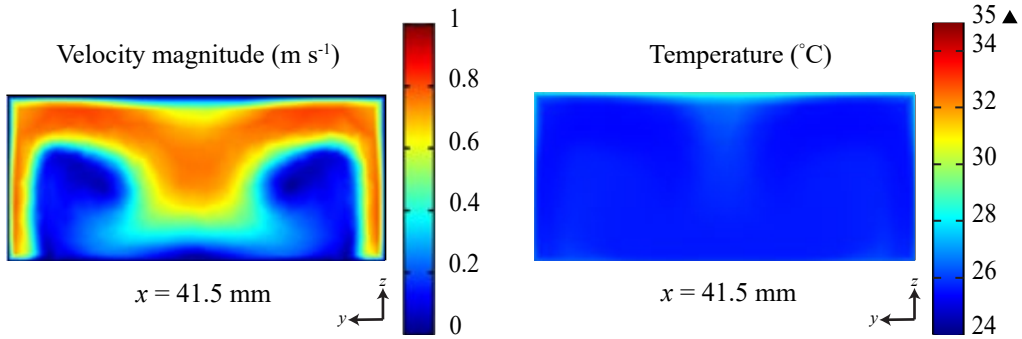

(b)

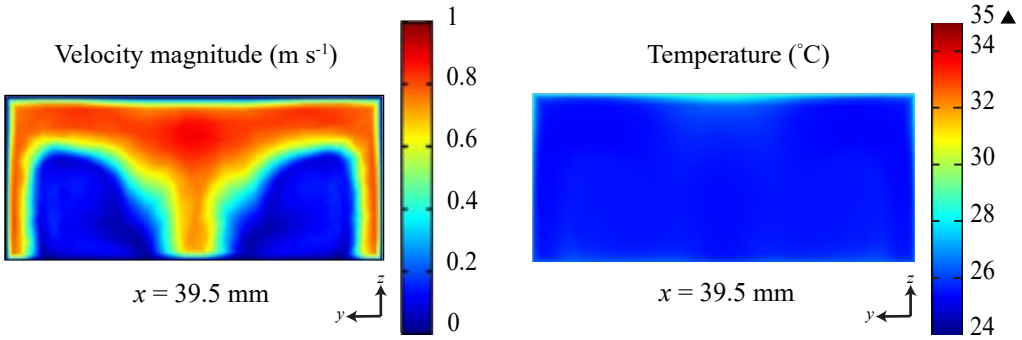

(c)

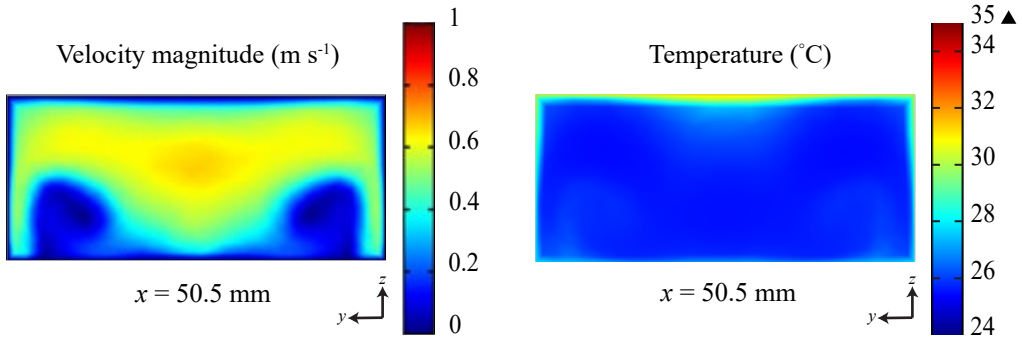

(d)

Figure 17: Velocity and temperature contours at $Re_{in} = 1,284$ (a) Prototype 1 (smooth channel). (b) Prototype 2 ($l = 3\,\text{mm}$, $\beta = 30°$, $H = 1.2\,\text{mm}$, $S = 18\,\text{mm}$). (c) Prototype 3 ($l = 2\,\text{mm}$, $\beta = 45°$, $H = 1.2\,\text{mm}$, $S = 17\,\text{mm}$). (d) Prototype 4 ($l = 2.5\,\text{mm}$, $\beta = 30°$, $H = 0.8\,\text{mm}$, $S = 22.5\,\text{mm}$)

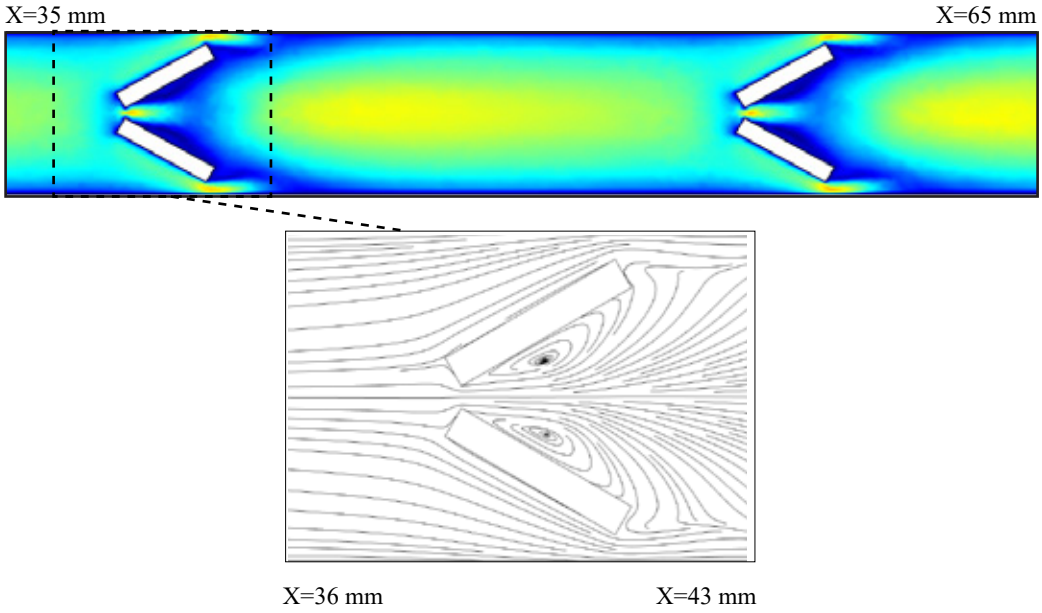

(a)

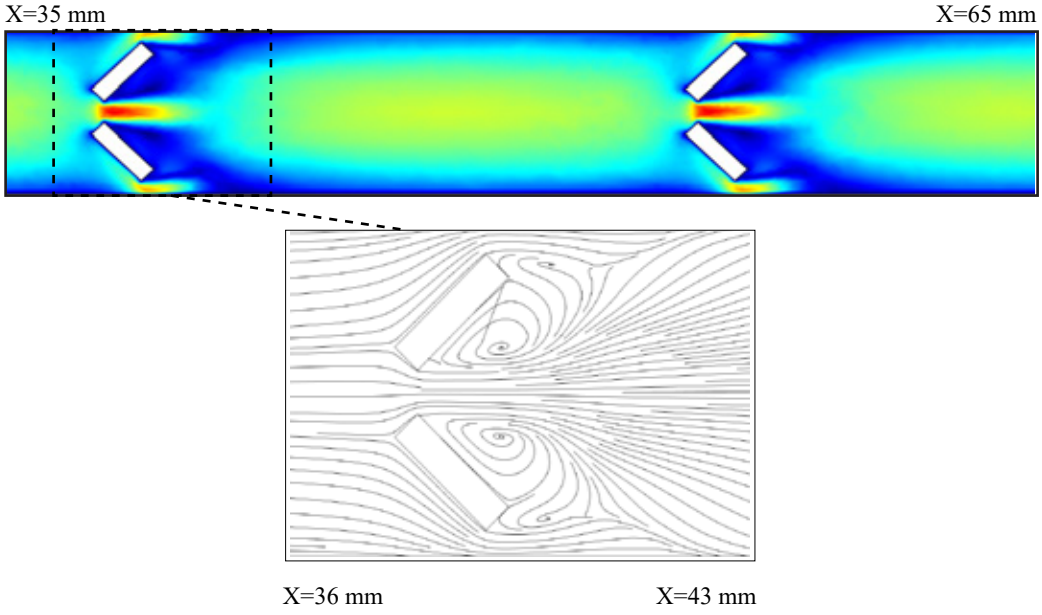

(b)

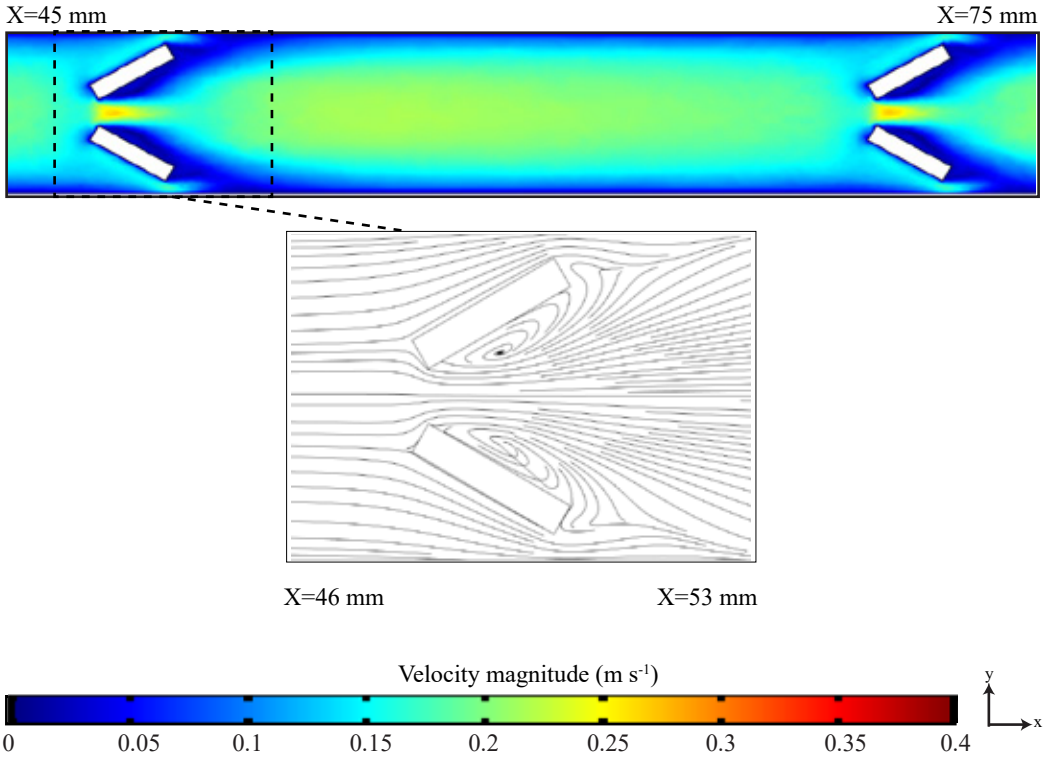

(c)

Figure 18: Velocity contours and streamlines at $Re_{in} = 481$ (a) Prototype 2 ($l = 3\,\text{mm}$, $\beta = 30°$, $H = 1.2\,\text{mm}$, $S = 18\,\text{mm}$). (b) Prototype 3 ($l = 2\,\text{mm}$, $\beta = 45°$, $H = 1.2\,\text{mm}$, $S = 17\,\text{mm}$). (c) Prototype 4 ($l = 2.5\,\text{mm}$, $\beta = 30°$, $H = 0.8\,\text{mm}$, $S = 22.5\,\text{mm}$)

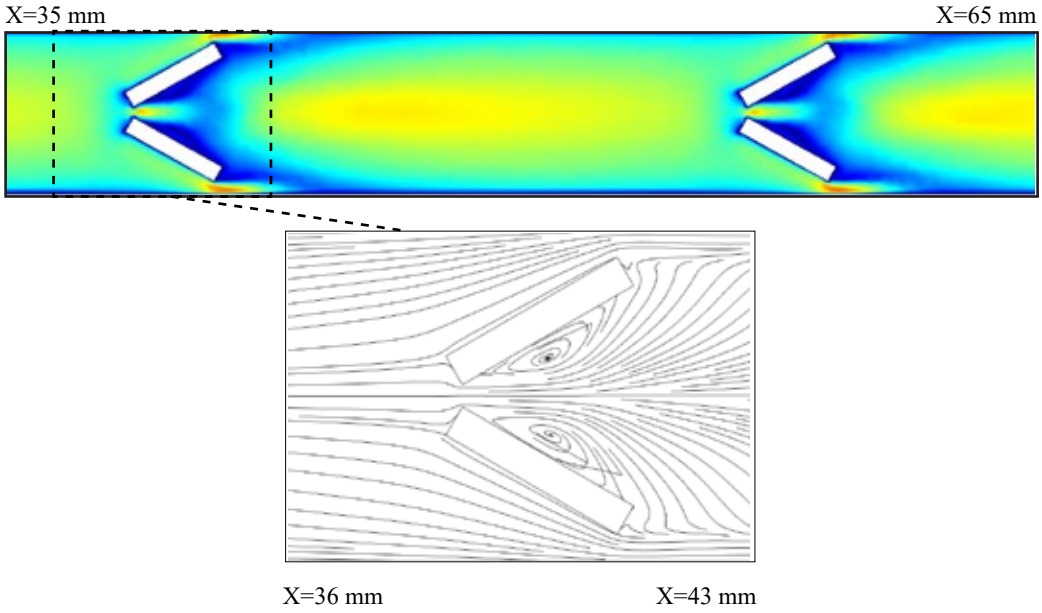

(a)

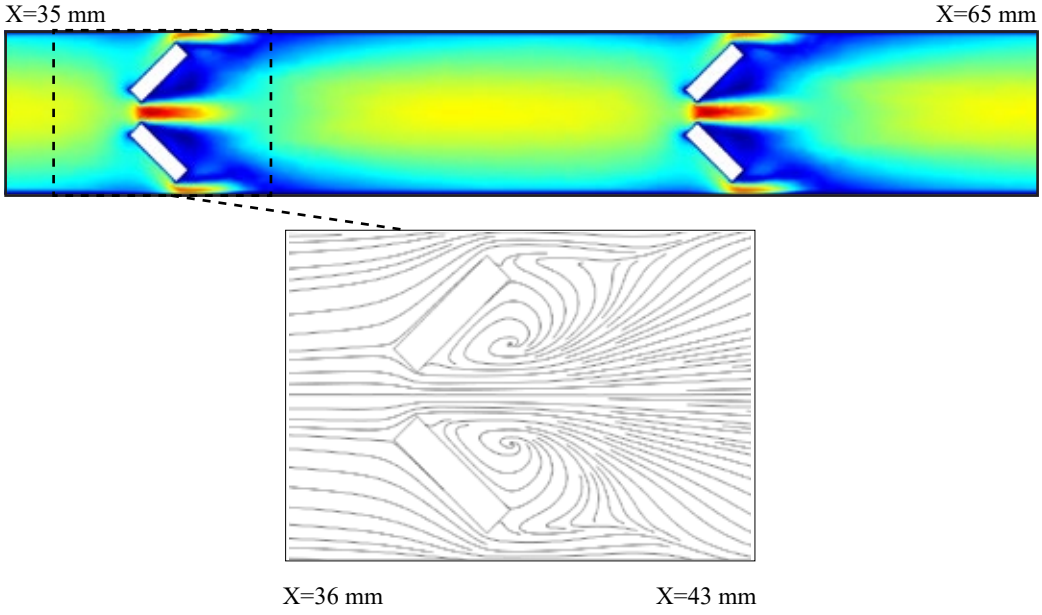

(b)

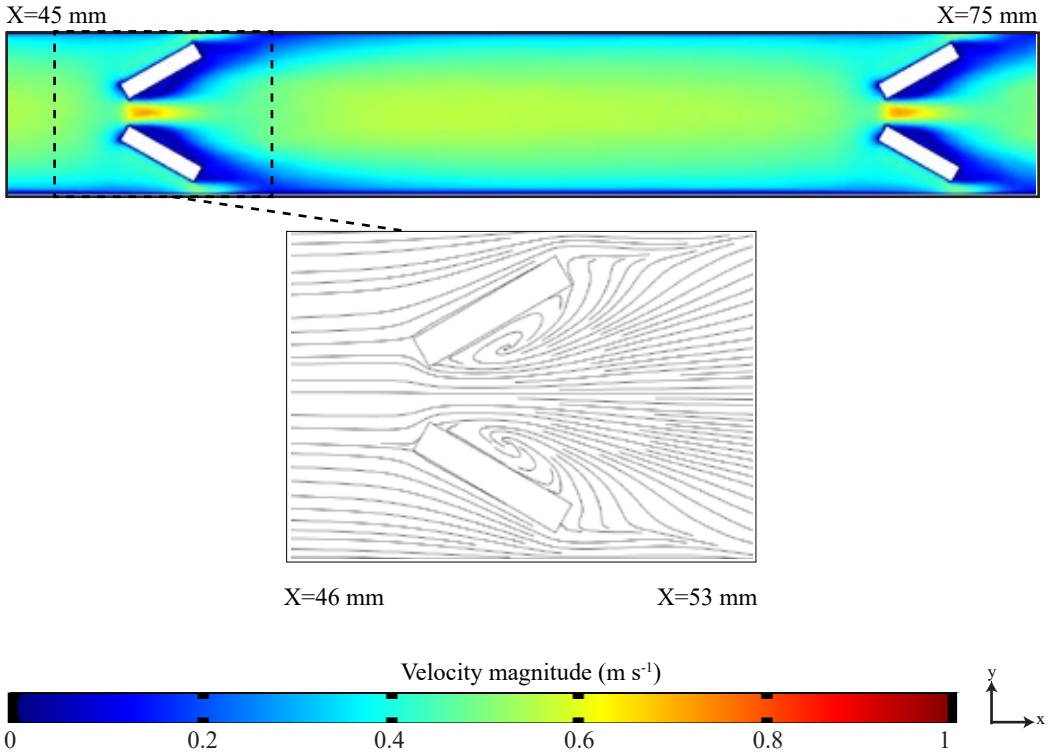

(c)

Figure 19: Velocity contours and streamlines at $Re_{in} = 1,284$ (a) Prototype 2 ($l = 3\,\text{mm}$, $\beta = 30°$, $H = 1.2\,\text{mm}$, $S = 18\,\text{mm}$). (b) Prototype 3 ($l = 2\,\text{mm}$, $\beta = 45°$, $H = 1.2\,\text{mm}$, $S = 17\,\text{mm}$). (c) Prototype 4 ($l = 2.5\,\text{mm}$, $\beta = 30°$, $H = 0.8\,\text{mm}$, $S = 22.5\,\text{mm}$)

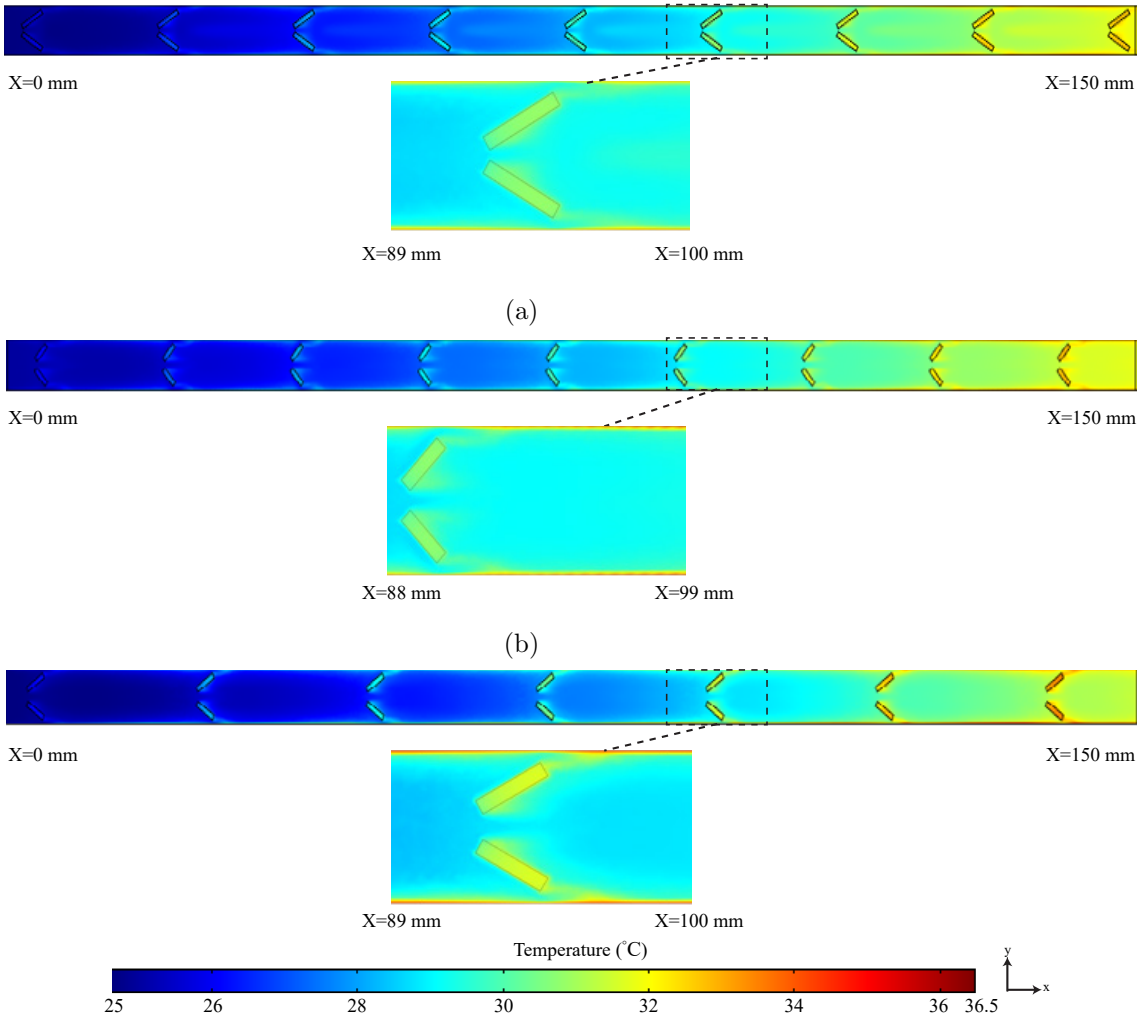

Figure 20: Temperature contours at $Re_{in} = 481$ (a) Prototype 2 ($l = 3\,\text{mm}$, $\beta = 30°$, $H = 1.2\,\text{mm}$, $S = 18\,\text{mm}$). (b) Prototype 3 ($l = 2\,\text{mm}$, $\beta = 45°$, $H = 1.2\,\text{mm}$, $S = 17\,\text{mm}$). (c) Prototype 4 ($l = 2.5\,\text{mm}$, $\beta = 30°$, $H = 0.8\,\text{mm}$, $S = 22.5\,\text{mm}$)

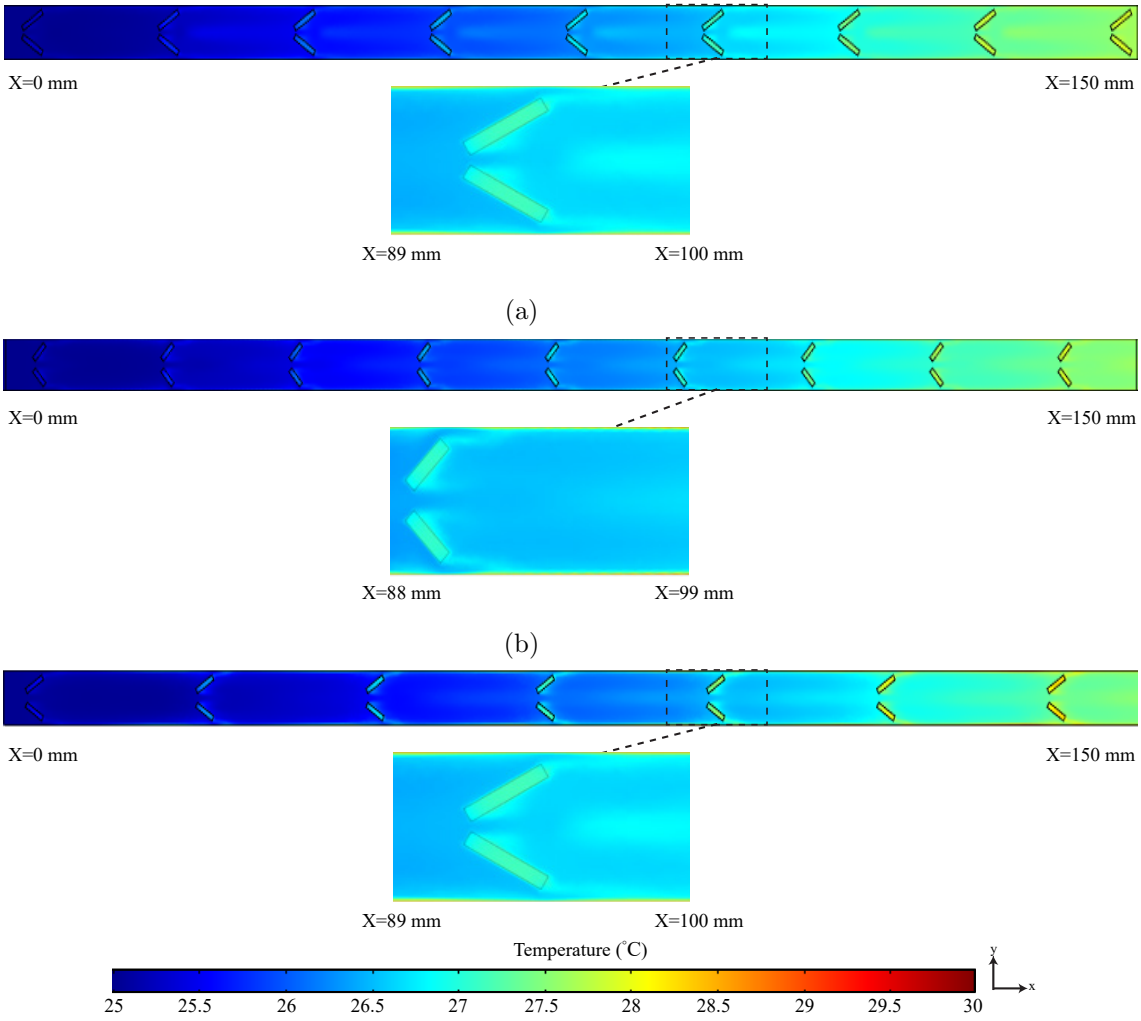

Figure 21: Temperature contours at $Re_{in} = 1,284$ (a) Prototype 2 ($l = 3\,\text{mm}$, $\beta = 30°$, $H = 1.2\,\text{mm}$, $S = 18\,\text{mm}$). (b) Prototype 3 ($l = 2\,\text{mm}$, $\beta = 45°$, $H = 1.2\,\text{mm}$, $S = 17\,\text{mm}$). (c) Prototype 4 ($l = 2.5\,\text{mm}$, $\beta = 30°$, $H = 0.8\,\text{mm}$, $S = 22.5\,\text{mm}$)

7. Conclusion

The main aim of the study was to investigate the feasibility of using metal three-dimensional (3D) printing as a manufacturing method to fabricate enhanced minichannel heat exchangers. The single-phase thermal characteristics of an enhanced minichannel heat exchanger equipped with longitudinal vortex generators were analyzed both experimentally and numerically. The minichannel heat exchangers were manufactured in an aluminum alloy (AlSi10Mg), according to desirable thermal features. Four different test sections including a smooth channel as a benchmark were printed via direct metal laser sintering (DMLS) technology owing to the better surface roughness and greater design uniformity. A proper test rig was developed to test the prototypes in the laminar flow condition using distilled water as a working fluid. The Reynolds number ranged from 170 to 1,380, and the heat exchangers were tested with two different heat fluxes of 15 $\mathrm{kW\,m^{-2}}$ and 30 $\mathrm{kW\,m^{-2}}$. The experimental conditions were used as an input for the numerical simulation using Comsol multiphysics as a tool. Also, extra simulations were conducted to have further understanding of the effect of the VGs inside the minichannel heat exchangers. The main conclusions of this research work are summarized as follows:

- The experimental results for smooth channel without vortex generators agreed well with the modified formula suggested by Hausen and a correlation developed by Lee and Garimella. While the correlations developed for fully developed velocity profile at the entrance and developing temperature profile predicted the obtained results reasonably well, the classical formula suggested for developing velocity and temperature profiles, over- predicted

the average Nusselt number with the current minichannel design and test setup.

- In the case of the channel equipped with vortex generators, COMSOL Multiphysics predicted the heat transfer coefficient reasonably well, and therefore it could be used in the ensuing analysis of 3D conjugate heat transfer in laminar flow.
- At the highest tested Reynolds number ($Re \approx 1380$) for Prototype 2, the convective heat transfer was almost three times that of the smooth channel. Therefore, vortex generators can be applied to the liquid side of the minichannel heat exchanger to boost convection. The three-dimensionally induced vortices caused by the vortex generators can significantly enhance the thermal characteristics, thereby potentially reducing the heat exchanger size for a given heat load.
- Finally, the verified thermal performance of the 3D-printed minichannel heat exchanger through both experimental and numerical calculations showed that additive manufacturing is a promising solution for the development of future enhanced minichannel heat exchangers.

Appendix A. Prototypes based on different metal AM method

In the earliest design phase, in order to find the proper metal 3D-printing method for manufacturing minichannel HXs, prototypes were developed using EBM and DMLS technologies. The prototypes were printed using ARCAM A2X (EBM) and EOS M290 (DMLS) metal AM machines. It was found that the channels could become blocked by unmelted powder in the case of EBM when the channel size was below 1.5 mm. Although detailed

surface roughness measurements were not conducted, the surface quality was found to be much lower for EBM than for DMLS. In conclusion, DMLS technology is promising for printing HXs, while EBM may have application for high-temperature gas HXs. The following figures show the printed prototypes.

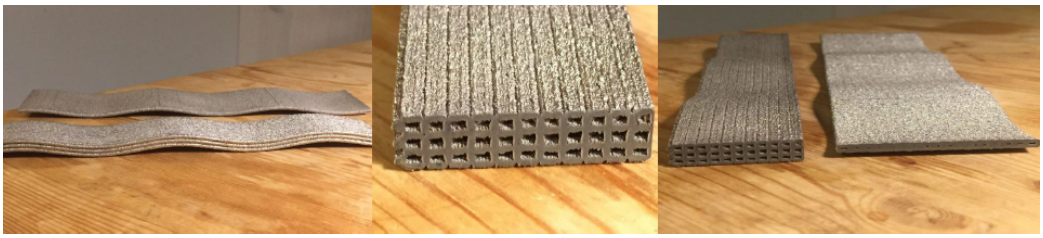

(a)

(b)

Figure 22: Various minichannels printed via different technologies. (a) with Arcam EBM machine in Inconel 718, (b) with EOS M290 DMLS in AlSi10Mg.

Appendix B. Exercising various heat transfer enhancement technique

In the next step and after finding DMLS technique an appropriate method for the production of heat exchangers, various enhancement techniques were exercised in order to attain a solid experience about the accuracy of metal 3D printers. Figure 23 demonstrates the printed part with DMLS technolgy in AlSi10Mg. It should be mentioned that the numerical parametric study of VG's effect in an additively manufactured minichannel heat exchanger was conducted based on the accuracy of this prototype [44].

Figure 23: Various passive enhancement techniques printed in AlSi10Mg using the DMLS fabrication method.

Appendix C. Surface roughness measurement

The surface roughness of each printed channels was measured via Stylus profiler (KLA-Tencor P-15). The result of roughness height is illustrated in Fig. 24 for each prototype. The arithmetic mean roughness R_a and the RMS roughness R_q were calculated according to the following equations:

$$R_a = \frac{1}{n}\sum_{i=1}^{n}|z_i - z_m| \tag{23}$$

$$R_q = \sqrt{\frac{1}{n}\sum_{i=1}^{n}(z_i - z_m)^2} \tag{24}$$

Where n is number of data points, z is the roughness height corresponding to each measured points, and z_m is a averaged roughness height of all measured points.

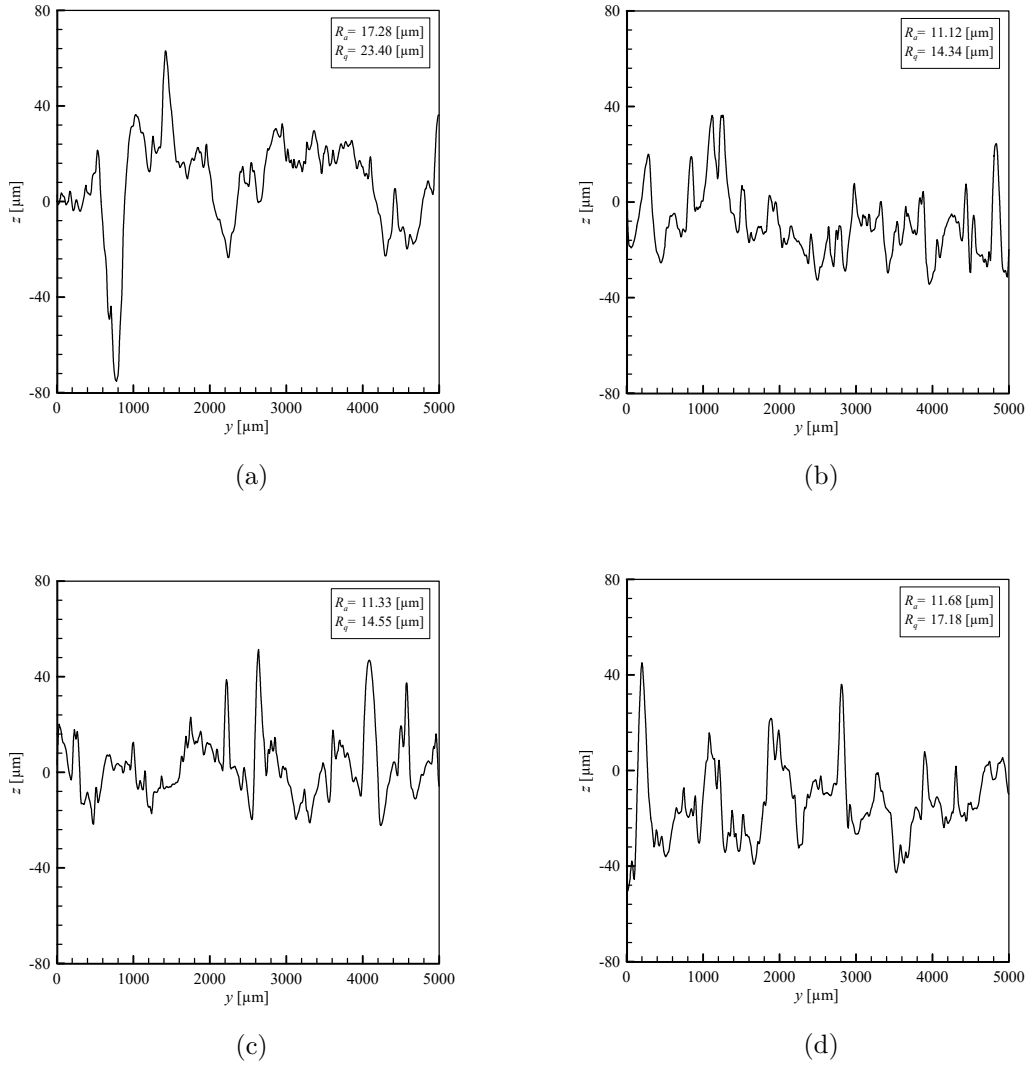

Figure 24: Surface roughness results: (a) Prototype 1 (smooth channel). (b) Prototype 2 ($l = 3\,\text{mm}$, $\beta = 30°$, $H = 1.2\,\text{mm}$, $S = 18\,\text{mm}$). (c) Prototype 3 ($l = 2\,\text{mm}$, $\beta = 45°$, $H = 1.2\,\text{mm}$, $S = 17\,\text{mm}$). (d) Prototype 4 ($l = 2.5\,\text{mm}$, $\beta = 30°$, $H = 0.8\,\text{mm}$, $S = 22.5\,\text{mm}$)

Declaration of interest

The authors declare that they have no known competing financial interests or personal relationships that could have appeared to influence the work reported in this paper.

Acknowledgement

Computations were performed on resources kindly provided by the Swedish National Infrastructure for Computing (SNIC) at PDC Centre for High Performance Computing (PDC-HPC).

References

[1] BP Energy Outlook, Tech. rep., British Petroleum (2019).
URL https://www.bp.com/content/dam/bp/business-sites/en/global/corporate/pdfs/energy-economics/energy-outlook/bp-energy-outlook-2019.pdf

[2] I. Dincer, M. A. Rosen, Energy, environment and sustainable development, Applied Energy 64 (1-4) (1999) 427–440. doi:10.1016/S0306-2619(99)00111-7.

[3] T. Dixit, I. Ghosh, Review of micro- and mini-channel heat sinks and heat exchangers for single phase fluids, Renewable and Sustainable Energy Reviews 41 (2015) 1298–1311. doi:10.1016/j.rser.2014.09.024.

[4] A. M. Omer, Energy, environment and sustainable development, Renewable and Sustainable Energy Reviews 12 (9) (2008) 2265–2300. doi:10.1016/j.rser.2007.05.001.

[5] R. Tiwari, R. S. Andhare, A. Shooshtari, M. Ohadi, Development of an additive manufacturing-enabled compact manifold microchannel heat exchanger, Applied Thermal Engineering 147 (2019) 781–788. doi:10.1016/j.applthermaleng.2018.10.122.

[6] S. G. Kandlikar, Fundamental issues related to flow boiling in minichannels and microchannels, Experimental Thermal and Fluid Science 26 (2) (2002) 389–407. doi:10.1016/S0894-1777(02)00150-4.

[7] D. B. Tuckerman, R. F. W. Pease, High-performance heat sinking for vlsi, IEEE Electron Device Letters 2 (5) (1981) 126–129. doi:10.1109/EDL.1981.25367.

[8] R. W. Knight, J. S. Goodling, B. E. Gross, Optimal thermal design of air cooled forced convection finned heat sinks-experimental verification, in: Proceeding of the Intersociety Conference on Thermal Phenomena in Electronic Systems, 1992, pp. 206–212. doi:10.1109/ITHERM.1992.187765.

[9] W. Qu, I. Mudawar, Analysis of three-dimensional heat transfer in micro-channel heat sinks, International Journal of Heat and Mass Transfer 45 (19) (2002) 3973–3985. doi:10.1016/S0017-9310(02)00101-1.

[10] P.-S. Lee, S. V. Garimella, D. Liu, Investigation of heat transfer in rectangular microchannels, International Journal of Heat and Mass Transfer 48 (9) (2005) 1688–1704. doi:10.1016/j.ijheatmasstransfer.2004.11.019.

[11] A. Weisberg, H. H. Bau, J. Zemel, Analysis of microchannels for integrated cooling, International Journal of Heat and Mass Transfer 35 (10) (1992) 2465–2474. doi:10.1016/0017-9310(92)90089-B.

[12] E. C. Forrest, L.-W. Hu, J. Buongiorno, T. J. McKrell, Convective heat transfer in a high aspect ratio minichannel heated on one side, Journal of Heat Transfer 138 (2) (2015) 21704–21710. doi:http://dx.doi.org/10.1115/1.4031646.

[13] P. Fernando, B. Palm, P. Lundqvist, E. Granryd, Propane heat pump with low refrigerant charge: design and laboratory

tests, International Journal of Refrigeration 27 (7) (2004) 761–773. doi:10.1016/j.ijrefrig.2004.06.012.

[14] P. Hrnjak, A. D. Litch, Microchannel heat exchangers for charge minimization in air-cooled ammonia condensers and chillers, International Journal of Refrigeration 31 (4) (2008) 658–668. doi:10.1016/j.ijrefrig.2007.12.012.

[15] H. A. Stone, A. D. Stroock, A. Ajdari, Engineering flows in small devices: microfluidics toward a lab-on-a-chip, Annu. Rev. Fluid Mech. 36 (2004) 381–411. doi:10.1146/annurev.fluid.36.050802.122124.

[16] A. Bergles, Heat transfer enhancement—the encouragement and accommodation of high heat fluxes, Journal of Heat Transfer 119 (1) (1997) 8–19. doi:https://doi.org/10.1115/1.2824105.

[17] M. E. Steinke, S. G. Kandlikar, Single-phase heat transfer enhancement techniques in microchannel and minichannel flows, in: ASME 2004, Proceeding of the 2nd International Conference on Microchannels and Minichannels, American Society of Mechanical Engineers, 2004, pp. 141–148. doi:10.1115/ICMM2004-2328.

[18] K. Navickaitė, A. Mocerino, L. Cattani, F. Bozzoli, C. Bahl, K. Liltrop, X. Zhang, K. Engelbrecht, Enhanced heat transfer in tubes based on vascular heat exchangers in fish: Experimental investigation, International Journal of Heat and Mass Transfer 137 (2019) 192–203. doi:10.1016/j.ijheatmasstransfer.2018.09.003.

[19] M. Fiebig, Vortices, generators and heat transfer, Chemical Engineering Research and Design 76 (2) (1998) 108–123. doi:10.1205/026387698524686.

[20] M. Fiebig, Embedded vortices in internal flow: heat transfer and pressure loss enhancement, International Journal of Heat and Fluid Flow 16 (5) (1995) 376–388. doi:10.1016/0142-727X(95)00043-P.

[21] G. Biswas, H. Chattopadhyay, Heat transfer in a channel with built-in wing-type vortex generators, International Journal of Heat and Mass Transfer 35 (4) (1992) 803–814. doi:10.1016/0017-9310(92)90248-Q.

[22] M. Fiebig, U. Brockmeier, N. Mitra, T. Gü Termann, Structure of velocity and temperature fields in laminar channel flows with longitudinal vortex generators, Numerical Heat Transfer 15 (3) (1989) 281–302. doi:https://doi.org/10.1080/10407788908944689.

[23] G. Biswas, K. Torii, D. Fujii, K. Nishino, Numerical and experimental determination of flow structure and heat transfer effects of longitudinal vortices in a channel flow, International Journal of Heat and Mass Transfer 39 (16) (1996) 3441–3451. doi:https://doi.org/10.1016/0017-9310(95)00398-3.

[24] P. A. Eibeck, J. K. Eaton, Heat transfer effects of a longitudinal vortex embedded in a turbulent boundary layer, Journal of Heat Transfer 109 (1) (1987) 16–24. doi:https://doi.org/10.1115/1.3248039.

[25] A. M. Jacobi, R. K. Shah, Heat transfer surface enhancement through the use of longitudinal vortices: A review of recent progress, Experimen-

tal Thermal and Fluid Science 11 (3) (1995) 295–309. doi:10.1016/0894-1777(95)00066-U.

[26] T. R. Johnson, P. N. Joubert, The Influence of Vortex Generators on the Drag and Heat Transfer From a Circular Cylinder Normal to an Airstream, Journal of Heat Transfer 91 (1) (1969) 91. doi:https://doi.org/10.1115/1.3580126.

[27] M. Fiebig, P. Kallweit, N. Mitra, S. Tiggelbeck, Heat transfer enhancement and drag by longitudinal vortex generators in channel flow, Experimental Thermal and Fluid Science 4 (1) (1991) 103–114. doi:10.1016/0894-1777(91)90024-L.

[28] J. Wu, W. Tao, Numerical study on laminar convection heat transfer in a rectangular channel with longitudinal vortex generator. Part A: Verification of field synergy principle, International Journal of Heat and Mass Transfer 51 (5) (2008) 1179–1191. doi:10.1016/j.ijheatmasstransfer.2007.03.032.

[29] J. Wu, W. Tao, Numerical study on laminar convection heat transfer in a channel with longitudinal vortex generator. part b: Parametric study of major influence factors, International Journal of Heat and Mass Transfer 51 (13-14) (2008) 3683–3692. doi:10.1016/j.ijheatmasstransfer.2007.03.031.

[30] C. Liu, J. tong Teng, J.-C. Chu, Y. lang Chiu, S. Huang, S. Jin, T. Dang, R. Greif, H.-H. Pan, Experimental investigations on liquid flow and heat transfer in rectangular microchannel with longitudinal vortex genera-

tors, International Journal of Heat and Mass Transfer 54 (13) (2011) 3069–3080. doi:10.1016/j.ijheatmasstransfer.2011.02.030.

[31] C. Chen, J.-T. Teng, C.-H. Cheng, S. Jin, S. Huang, C. Liu, M.-T. Lee, H.-H. Pan, R. Greif, A study on fluid flow and heat transfer in rectangular microchannels with various longitudinal vortex generators, International Journal of Heat and Mass Transfer 69 (2014) 203–214. doi:10.1016/j.ijheatmasstransfer.2013.10.018.

[32] A. Datta, D. Sanyal, A. K. Das, Numerical investigation of heat transfer in microchannel using inclined longitudinal vortex generator, Applied Thermal Engineering 108 (2016) 1008–1019. doi:10.1016/j.applthermaleng.2016.07.165.

[33] A. Ebrahimi, E. Roohi, S. Kheradmand, Numerical study of liquid flow and heat transfer in rectangular microchannel with longitudinal vortex generators, Applied Thermal Engineering 78 (2015) 576–583. doi:10.1016/j.applthermaleng.2014.12.006.

[34] S. G. Kandlikar, W. J. Grande, Evolution of microchannel flow passages–thermohydraulic performance and fabrication technology, Heat Transfer Engineering 24 (1) (2003) 3–17. doi:https://doi.org/10.1080/01457630304040.

[35] I. L. Collins, J. A. Weibel, L. Pan, S. V. Garimella, A permeable-membrane microchannel heat sink made by additive manufacturing, International Journal of Heat and Mass Transfer 131 (2019) 1174–1183. doi:10.1016/j.ijheatmasstransfer.2018.11.126.

[36] C. K. Stimpson, J. C. Snyder, K. A. Thole, D. Mongillo, Scaling roughness effects on pressure loss and heat transfer of additively manufactured channels, Journal of Turbomachinery 139 (2) (2017) 021003. doi:https://doi.org/10.1115/1.4034555.

[37] I. L. Collins, J. A. Weibel, L. Pan, S. V. Garimella, Evaluation of additively manufactured microchannel heat sinks, IEEE Transactions on Components, Packaging and Manufacturing Technology 9 (3) (2019) 446–457. doi:10.1109/TCPMT.2018.2866972.

[38] K. L. Kirsch, K. A. Thole, Heat transfer and pressure loss measurements in additively manufactured wavy microchannels, Journal of Turbomachinery 139 (1) (2017) 011007. doi:https://doi.org/10.1115/1.4034342.

[39] K. L. Kirsch, K. A. Thole, Pressure loss and heat transfer performance for additively and conventionally manufactured pin fin arrays, International Journal of Heat and Mass Transfer 108 (2017) 2502–2513. doi:10.1016/j.ijheatmasstransfer.2017.01.095.

[40] M. A. Arie, A. H. Shooshtari, M. M. Ohadi, Experimental characterization of an additively manufactured heat exchanger for dry cooling of power plants, Applied Thermal Engineering 129 (2018) 187–198. doi:10.1016/j.applthermaleng.2017.09.140.

[41] T. L. Bergman, F. P. Incropera, D. P. DeWitt, A. S. Lavine, Fundamentals of heat and mass transfer, seventh Edition, John Wiley & Sons, 2011.

[42] S. G. Kandlikar, Chapter 3 - single-phase liquid flow in minichannels and microchannels, in: S. G. Kandlikar, S. Garimella, D. Li, S. Colin, M. R. King (Eds.), Heat Transfer and Fluid Flow in Minichannels and Microchannels, 2nd Edition, Butterworth-Heinemann, Oxford, 2014, pp. 103–174. doi:https://doi.org/10.1016/B978-0-08-098346-2.00003-X.
URL http://www.sciencedirect.com/science/article/pii/B978008098346200003X

[43] M. Khoshvaght-Aliabadi, M. Sahamiyan, M. Hesampour, O. Sartipzadeh, Experimental study on cooling performance of sinusoidal–wavy minichannel heat sink, Applied Thermal Engineering 92 (2016) 50–61. doi:10.1016/j.applthermaleng.2015.09.015.

[44] H. Rastan, T. Ameel, B. Palm, Parametric study of vortex generator effects in an additive manufactured minichannel heat exchanger, in: ASME 2019, Proceeding of the 17th International Conference on Nanochannels, Microchannels, and Minichannels, American Society of Mechanical Engineers Digital Collection, 2019. doi:10.1115/ICNMM2019-4236.

[45] R. K. Roy, A primer on the Taguchi method, 2nd Edition, Society of Manufacturing Engineers, 2010.

[46] H. Rastan, A. Abdi, M. Ignatowicz, B. Hamawandi, P. S. Lee, B. Palm, Heat transfer investigation of an additively manufactured minichannel heat exchanger, in: ASME 2019, Proceeding of the 17th International Conference on Nanochannels, Microchannels, and Minichan-

nels, American Society of Mechanical Engineers Digital Collection, 2019. doi:10.1115/ICNMM2019-4231.

[47] W. Wagner, H.-J. Kretzschmar, International Steam Tables-Properties of Water and Steam based on the Industrial Formulation IAPWS-IF97, Springer Science & Business Media, 2007. doi:10.1007/978-3-540-74234-0.

[48] S. Zeng, B. Kanargi, P. S. Lee, Experimental and numerical investigation of a mini channel forced air heat sink designed by topology optimization, International Journal of Heat and Mass Transfer 121 (2018) 663–679. doi:10.1016/j.ijheatmasstransfer.2018.01.039.

[49] F. Stern, M. Muste, M.-L. Beninati, W. E. Eichinger, Summary of experimental uncertainty assessment methodology with example, Tech. rep., IIHR Report (1999).

[50] R. J. Moffat, Describing the uncertainties in experimental results, Experimental Thermal and Fluid Science 1 (1) (1988) 3–17. doi:10.1016/0894-1777(88)90043-X.

[51] R. Dieck, W. Steele, G. Osolsobe, Test uncertainty. asme ptc 19.1-2005, American Society of Mechanical Engineers, New York, NY (2005).

[52] S. Tiggelbeck, N. Mitra, M. Fiebig, Flow structure and heat transfer in a channel with multiple longitudinal vortex generators, Experimental Thermal and Fluid Science 5 (4) (1992) 425–436. doi:https://doi.org/10.1016/0894-1777(92)90029-5.

[53] T. Ma, X. Lu, J. Pandit, S. V. Ekkad, S. T. Huxtable, S. Deshpande, Q. wang Wang, Numerical study on thermoelectric–hydraulic performance of a thermoelectric power generator with a plate-fin heat exchanger with longitudinal vortex generators, Applied Energy 185 (2017) 1343–1354, clean, Efficient and Affordable Energy for a Sustainable Future. doi:10.1016/j.apenergy.2016.01.078.

[54] J. Ma, Y. P. Huang, J. Huang, Y. L. Wang, Q. W. Wang, Experimental investigations on single-phase heat transfer enhancement with longitudinal vortices in narrow rectangular channel, Nuclear Engineering and Design 240 (1) (2010) 92–102. doi:10.1016/j.nucengdes.2009.10.015.

[55] A. Abdollahi, M. Shams, Optimization of shape and angle of attack of winglet vortex generator in a rectangular channel for heat transfer enhancement, Applied Thermal Engineering 81 (2015) 376–387. doi:10.1016/j.applthermaleng.2015.01.044.

[56] J. Gorman, E. Sparrow, J. Ahn, In-line tube-bank heat exchangers: Arrays with various numbers of thermally participating tubes, International Journal of Heat and Mass Transfer 132 (2019) 837–847. doi:10.1016/j.ijheatmasstransfer.2018.11.167.

[57] J. Koo, C. Kleinstreuer, Viscous dissipation effects in microtubes and microchannels, International Journal of Heat and Mass Transfer 47 (14-16) (2004) 3159–3169. doi:10.1016/j.ijheatmasstransfer.2004.02.017.

[58] G. L. Morini, M. Spiga, The role of the viscous dissipation in

heated microchannels, Journal of heat transfer 129 (3) (2007) 308–318. doi:https://doi.org/10.1115/1.2430725.

[59] D. Gee, R. Webb, Forced convection heat transfer in helically rib-roughened tubes, International Journal of Heat and Mass Transfer 23 (8) (1980) 1127–1136. doi:10.1016/0017-9310(80)90177-5.
URL http://www.sciencedirect.com/science/article/pii/0017931080901775

[60] R. Webb, Performance evaluation criteria for use of enhanced heat transfer surfaces in heat exchanger design, International Journal of Heat and Mass Transfer 24 (4) (1981) 715–726. doi:10.1016/0017-9310(81)90015-6.
URL http://www.sciencedirect.com/science/article/pii/0017931081900156

[61] J.-Y. Yun, K.-S. Lee, Influence of design parameters on the heat transfer and flow friction characteristics of the heat exchanger with slit fins, International Journal of Heat and Mass Transfer 43 (14) (2000) 2529–2539. doi:10.1016/S0017-9310(99)00342-7.
URL http://www.sciencedirect.com/science/article/pii/S0017931099003427

[62] P.-S. Lee, S. V. Garimella, Thermally developing flow and heat transfer in rectangular microchannels of different aspect ratios, International Journal of Heat and Mass Transfer 49 (17) (2006) 3060–3067. doi:10.1016/j.ijheatmasstransfer.2006.02.011.

[63] H. D. Baehr, K. Stephan, Convective heat and mass transfer. Single phase flow, Springer Berlin Heidelberg, Berlin, Heidelberg, 2011, pp. 275–441. doi:https://doi.org/10.1007/978-3-642-20021-2_3.

[64] E. N. Sieder, G. E. Tate, Heat transfer and pressure drop of liquids in tubes, Industrial & Engineering Chemistry 28 (12) (1936) 1429–1435. doi:https://doi.org/10.1021/ie50324a027.